

Pinpointing energy transfer mechanisms in the quenching process of microwave air plasma

Q. Shen¹, A. Pikalev^{1,2}, F.J.J. Peeters³, V. Guerra², M.C.M. van de Sanden^{1,4,*}

1. Dutch Institute for Fundamental Energy Research, Eindhoven, The Netherlands

2. Instituto de Plasmas e Fusão Nuclear, Instituto Superior Técnico, Universidade de Lisboa, Lisboa, Portugal

3. Leyden Jar Company, Eindhoven, The Netherlands

4. Department of Applied Physics, Eindhoven Institute of Renewable Energy Systems, Eindhoven University of Technology, Eindhoven, The Netherlands

E-mail: M.C.M.vandeSanden@diffier.nl

Abstract. A time-dependent multi-temperature quenching model at atmospheric pressure, incorporating chemical and vibrational kinetics, is introduced. The model provides insights into the pathways of NO_x formation and destruction in the downstream region of a microwave air plasma. The relaxation of the temperatures during the forced cooling trajectory by the wall is modelled. A Continuous Stirred Tank Reactor model and a Plug Flow Reactor model represent the plasma and quenching regions, respectively. For the non-thermal conditions, where gas and vibrational temperatures differ, most reaction rate coefficients, except those obtained from molecular dynamics methods, are determined based on a generalized Fridman-Macheret scheme. The energy transfer channels involved in the quenching process are tracked across different time scales. By varying the gas temperature in the plasma region and the cooling rate, the reaction pathways for the NO_x synthesis mechanism are analysed. This research provides a first step for the further advancement and optimisation of plasma reactors for efficient NO_x production.

1. Introduction

Limited availability of natural nitrogen-based fertilizer has restrained agricultural productivity until the advent of the Haber-Bosch (H-B) process. Nowadays, the H-B process fixes approximately 130 million tons of nitrogen annually, sustaining over 40% of the global population [1, 2]. However, this process is currently one of the largest global energy consumers and greenhouse gas emitters, accounting for about 1.2% of the global anthropogenic CO_2 emissions, prompting researchers to recommend alternative Nitrogen Fixation (NF) methods [3]. Although major strides have been made to electrify the H-B process, it continues to rely heavily on fossil fuels and remains inflexible [4]. Recently, plasma technology has attracted more and more attention, as it can be easily switched on and off, making it compatible with fluctuating renewable energy sources such as

solar or wind power [5, 6]. Consequently, the plasma NF process has the potential to significantly reduce CO₂ emissions compared to traditional methods, paving the way for sustainable NF with net-zero emissions in the future [7–9].

Several articles have discussed the underlying NO_x synthesis mechanisms in different plasma types [5, 7, 10]. The most energy-efficient pathway for NO synthesis involves stimulating non-thermal processes through vibrational excitation, which is reported to have the potential to achieve a theoretical power consumption limit of 0.1 MJ/mol N⁻¹, *i.e.*, 2.5 times lower than that of the H-B process [11]. The highest NO production (14%) with the lowest energy cost (0.28 MJ/mol N⁻¹) was achieved by Asisov *et al.* employing a low-pressure (10–100 Torr) electron cyclotron resonance microwave (MW) discharge with a magnetic field and cryogenically cooled reactor wall [10, 12]. However, neither the energy consumed to sustain the low pressure in the reactor, nor the energy required for cooling the wall is included in the energy cost calculation [4, 13]. For other typical non-thermal plasmas, like dielectric barrier discharges, the energetic electrons, excited by the high reduced electric field (above 100 Td), spend too much energy on electronic excitation, ionisation, and dissociation, instead of vibrational excitation, resulting in a higher energy cost (18 MJ/mol N⁻¹) and low NO_x production [14].

Warm plasma is another promising option for NO_x synthesis, because it can provide a high ionisation degree, coupled with non-thermal effects (*i.e.*, selectively populate certain degrees of freedom, such as vibrationally excited states) [15]. Although the translational temperature in warm plasma is much lower than the electron temperature ($\sim 1\text{--}2$ eV), it is still significantly higher than room temperature, reaching several thousand Kelvin [14]. Kelly *et al.* [2] presented an atmospheric pressure MW plasma stabilised by a vortex gas flow, achieving an energy cost of 2 MJ/mol N⁻¹ and a NO_x production of 3.8%. Vervloessem *et al.* [16] reported NO_x formation of 1.5% at an energy cost of 3.6 MJ/mol N⁻¹ based on a gliding arc (GA) plasmatron at the same pressure. A lower energy cost (1.8 MJ/mol N⁻¹) was achieved by Tsonev *et al.* [17] using a rotating GA plasma reactor at elevated pressure. Still, the energy cost of NO_x synthesis in warm plasma remains high, because a high gas temperature is required to break the strong N-N chemical bonds, while NO is unstable at these elevated temperatures [5]. Furthermore, effective quenching is necessary to prevent the NO_x generated in the plasma zone from decomposing back into N₂ and O₂ [10]. There is ample literature debating NO_x formation and CO₂ dissociation mechanisms in plasmas, for sustainable chemistry applications. As it is also largely debated, the bottlenecks of those processes are the product quenching and separation of products [18–21]. Van Alphen *et al.* [18] indicated an 8% enhancement in NO_x concentration using a so-called ‘effusion nozzle’ in a rotating GA plasma reactor. Similarly, Majeed *et al.* [19] found that NO_x production increased by 12.4% when the mixture was mixed with a cold gas after the plasma zone in the same reactor. Therefore, exploring the underlying mechanisms in the quenching region is crucial for both future plasma reactor development and energy cost optimization.

Due to the short lifetimes of many intermediate products generated by plasma, a full understanding of NO_x synthesis through experiments is extremely demanding [11]. An accurate and comprehensive theoretical model allows researchers to gain a deeper and more quantitative knowledge of the plasma NF process [22]. Altin *et al.* [23] developed a zero-dimensional (0D) chemistry model to investigate vibrational excitation in the core of pure N_2 MW plasmas, with pressure varying from 50 to 400 mbar. In a follow-up paper, a one-dimensional (1D) radial fluid model revealed the gas heating mechanism of the plasma core and its outer region in pure N_2 MW plasma [24]. Based on a 0D chemical kinetics model, Wang *et al.* [5] illustrated the NO_x synthesis in a GA plasma at atmospheric pressure. The results revealed that the vibrational excitation of N_2 can lower the high energy barrier for N_2 dissociation, thereby reducing the energy cost of the NF process. In another 0D chemical kinetics model for a reverse-vortex flow GA plasmatron at atmospheric pressure, Vervloessem *et al.* [16] reported that the energy cost could potentially be reduced to $0.5 \text{ MJ/mol N}^{-1}$ by preventing the transfer of vibrational energy from N_2 to O_2 . The strong non-equilibrium effects in high-enthalpy gas flows expanding through nozzles have been investigated. Kustova *et al.* [25] examined how different vibrational distributions affect heat transfer and diffusion in expanding nozzle flows using various kinetic models. Shizgal *et al.* [26] found that the forward rates of $\text{O}_2\text{--O}_2$ and $\text{O}_2\text{--O}$ dissociation reactions in hypersonic nozzle expansion significantly deviate from equilibrium due to vibrational nonequilibrium effects. The calculations showed that near the throat, all vibrational levels contribute to the forward reaction rates, whereas farther downstream, the highest vibrational levels dominate. Cutler *et al.* [27] experimentally and computationally investigated vibrational and rotational temperatures in a Mach 2 nozzle, showing vibrational freezing effects and the role of steam in promoting thermal equilibrium.

In this work, we concentrate on the quenching of air activated by warm plasma using a time-dependent multi-temperature quenching model, which is coupled with chemical and vibrational kinetics under atmospheric pressure, allowing for the study of the underlying mechanisms. Overall, the model provides a first step for understanding the quenching process in the downstream afterglow of a MW air plasma, revealing the intricate balance of energy input, cooling rates, and chemical-kinetical reactions. This insight is crucial for optimizing NO_x production while minimizing energy costs, laying the groundwork for further advancements in plasma-based nitrogen fixation technologies.

2. Model description

In order to better understand the NO_x formation and energy exchange mechanisms in the MW plasma, a 0D Continuous Stirred Tank Reactor (CSTR) model coupled with a 1D axial Plug Flow Reactor (PFR) model is employed to represent the plasma region and quenching region, respectively, as shown in Figure 1. During the discharge, 10 slm air (79% N_2 and 21% O_2) undergoes numerous physical and chemical processes, including electronic and vibrational excitation, ionisation, dissociation, and

recombination [11]. Since experiments using Raman spectroscopy have shown that the vibrational temperature is very close to the rotational temperature in the core of microwave air plasma at 650 mbar [28], it is valid to assume that the gas mixture is in thermal equilibrium in the plasma region at atmospheric pressure, and can be represented by a CSTR model. The residence time in the CSTR model is a critical factor affecting the performance [29, 30], particularly at low pressure. The length of the CSTR—the parameter governing the residence time—is fixed at 4 cm. Because the gas mixture reaches chemical equilibrium very fast under atmospheric pressure, a sensitivity test has confirmed that the length of the CSTR has a limited effect on the result when the temperature in the CSTR (T_{CSTR}) is beyond 2500 K (Figure S1 in Supplementary material). Therefore, it is reasonable to assume that the initial gas reaches the chemical equilibrium based on the gas temperature in the CSTR model. Note that the calculations using the CSTR, which simulate the microwave plasma, only provide the initial conditions for our analysis of the quenching process in the afterglow and do not influence the analysis of energy transfer during quenching.

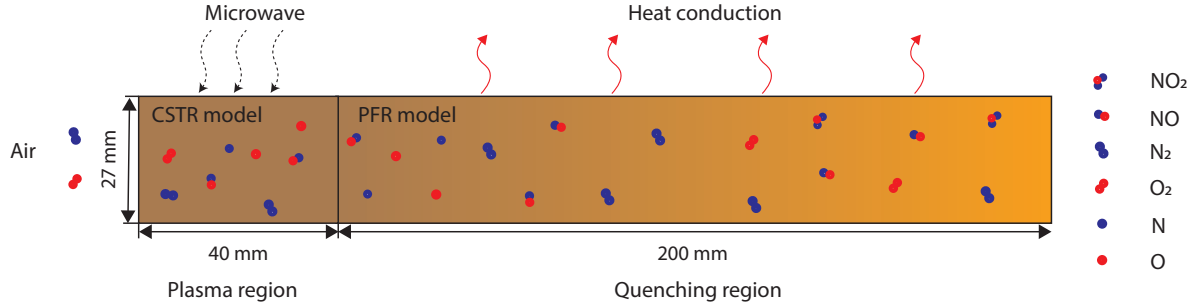


Figure 1: Sketch of the complete model in this work.

The PFR model is represented by a series of small CSTRs connected in sequence. This approach assumes that the quenching region can be approximated by dividing it into numerous smaller compartments [31]. Each CSTR represents a small volume within the PFR, where perfect mixing is assumed within that compartment, but not between different compartments. The gas mixture entering the first CSTR has the specified inlet composition from the plasma region, while for all subsequent CSTRs, the inlet composition is fixed to match the reactor immediately upstream [32]. The PFR model typically assumes the fluid is perfectly mixed in the radial direction, which means that the density profiles of each component are uniform across the direction perpendicular to the axis [33]. In a PFR model, where diffusion is absent, upstream reactors are unaffected by downstream reactors. Consequently, the problem can be solved by sequentially progressing from the first reactor to the last, integrating each into a steady state [32]. The residence time of each step depends on the mass flow rate and the 0D reactor volume. By increasing the number of CSTRs, the model can capture the gradients in concentration or temperature across the reactor length. In this work, the length of each compartment in the PFR is variable. When any temperature

difference—whether in gas temperature or in the vibrational temperatures of N_2 and O_2 —between the current and previous compartment falls below 1 K or exceeds 10 K, the model recalculates the current step by adjusting the reactor length until the result meets the specified criteria, thus improving computational efficiency. The simulation continues until the cumulative length of all compartments reaches or exceeds 20 cm, after which all active species are depleted under all investigated conditions (the reaction $2\text{NO} + \text{O}_2 \rightarrow 2\text{NO}_2$ is active at longer times and is discussed separately). Consequently, the number of compartments in the PFR reactor varies under different conditions. Moreover, because species concentrations at atmospheric pressure in the MW reactor are primarily determined by gas-phase chemistry [34], surface reactions are not included in the model.

Since the translational relaxation time is shorter than the vibrational-translational relaxation time, apart from the plasma region, fast cooling in the quenching region is another possible way to achieve non-thermal effects, which might benefit NO production. The vibrational modes of N_2 and O_2 are assumed to follow a Boltzmann distribution controlled by their vibrational temperatures. As a result, nearly all reactions that involve O_2 or N_2 as a reactant can be vibrationally stimulated (*i.e.*, reactions $X_1^f - X_5^f$ in Table 1). The model is implemented using Cantera, an open-source Python package that solves chemical kinetics, thermodynamics, and transport processes [32].

Several aspects demonstrate the accuracy and reliability of the present model. Firstly, the accuracy of the generalized Fridman-Macheret method used in this work has been proved by comparison with Quasi-Classical Trajectory (QCT) results [35, 36]. Secondly, the predicted molar fractions with sufficient residence time in the CSTR show excellent agreement with those obtained from chemical equilibrium [37]. Thirdly, under low cooling rate conditions, the model correctly predicts the absence of non-thermal equilibrium effects, consistent with experimental observations even at lower pressures [28]. Lastly, in high-enthalpy nozzle flows, a higher vibrational temperature is observed compared to the gas temperature, aligning with the prediction of the present model that stronger non-thermal effects persist under high cooling rates [25–27].

2.1. Chemistry set

Given that minimal N_2O , N_2O_3 , or N_2O_4 is observed in the experiments [2], these species are omitted from the reaction model. Table 1 lists all chemical reactions included in the model. For the reactions X_2^f and X_5^f , the thermal reaction rate coefficients are calculated by the molecular dynamics (MD) data [38–40]:

$$k = \sum_v f_v(T_g) \sum_w k_{v,w}(T_g) \quad (1)$$

where $f_v(T_g)$ is the Boltzmann factor of O_2 or N_2 [41], $k_{v,w}(T_g)$ is the state-specific rate coefficient for v^{th} vibrational state of N_2 or O_2 as the reactant, and w^{th} level of NO as the product. More information can be found in the work of Armenise *et al.* [38–40]. The thermal rate coefficients of the reaction $\text{O}_2 + \text{O}_2/\text{O}$ in reaction X_1^f and $\text{N}_2 + \text{N}_2/\text{N}$ in

reaction X_4^f are calculated by the QCT data [35, 36, 42]:

$$k = \sum_v f_v(T_g) k_v(T_g) \quad (2)$$

For the other reactions in Table 1, all the forward rate coefficients (X^f) in thermal equilibrium are calculated using the modified Arrhenius form [32]:

$$k = AT_g^b \exp\left(-\frac{E_a}{k_B T_g}\right) \quad (3)$$

where k [m^3s^{-1}] is the reaction rate coefficient, A [m^3s^{-1}] is the pre-exponential factor, k_B is the Boltzmann constant, b is the temperature exponent, T_g [K] is the gas temperature, and E_a [eV] is the activation energy.

All rate coefficients for the backward reactions are determined by detailed balance, (*i.e.*, the net rate-of-progress of all reactions is zero [34]). The relation between the forward and backward rate coefficients is expressed by:

$$K_{eq,i} \equiv \frac{k_{f,i}}{k_{b,i}} \quad (4)$$

where $K_{eq,i}$ is the equilibrium constant of the reaction i , calculated using the formula known from thermodynamics [43]:

$$K_{eq,i} = \left(\frac{P_{ref}}{k_B T_g}\right)^{\sum_j a_{ij}} \exp\left(-\frac{\sum_j a_{ij} G_{ij}^{ref}(T_g)}{RT_g}\right) \quad (5)$$

where a_{ij} is the stoichiometric factors of species j (positive for products and negative for reactants) of each chemical component in the corresponding process, the sums are taken over all components that take part in the given reaction; G_{ij}^{ref} [$\text{J}\cdot\text{mol}^{-1}$] are the molar Gibbs energies of components at the reference pressure P_{ref} [Pa]; R is gas constant.

It is worth emphasizing that QCT is primarily used in atom-molecule collisions [35, 36]. For molecule-molecule collisions, as detailed by Andrienko *et al.* [48], there are insufficient QCT data available for modelling. Therefore, a semi-empirical scaling of QCT atom-molecule dissociation data is applied to the calculation of rate coefficients for molecule-molecule collisions. All QCT molecule-molecule collision data are sourced from the work of Esposito *et al.* [35] and Andrienko *et al.* [42].

The total non-thermal rate coefficients for all forward Zeldovich reactions (X_2^f , and X_5^f) are calculated using Eq.1, with the Boltzmann factor determined by the vibrational temperature. Likewise, the Boltzmann factor in Eq.2 is modified to calculate the total non-thermal rate coefficients for the reactions $\text{O}_2 + \text{O}_2/\text{O}$ in reaction X_1^f and $\text{N}_2 + \text{N}_2/\text{N}$ in reaction X_4^f . Based on the comparison by Lino da Silva *et al.*, the Fridman-Macheret method provides more accurate results for calculating non-thermal rate coefficients than other two-temperature methods [49]. Therefore, a generalized Fridman-Macheret method is employed to compute the total non-thermal rate coefficients for reaction X_3^f and the remaining parts of X_1^f and X_4^f , as given by:

$$k_{non}^{total}(T_g, T_v) = \frac{AT_g^b e^{\frac{-E_a}{k_B T_g}} Z(T_g) \sum_v^{max} e^{\left(\frac{-E_v}{k_B T_v} + \frac{\alpha E_v^*}{k_B T_g}\right)}}{Z(T_v) \sum_v^{max} e^{\frac{-(E_v - \alpha E_v^*)}{k_B T_g}}} \quad (6)$$

Table 1: List of thermal chemistry reactions. All the rate coefficients for the backward reactions are determined by the principle of detailed balance.

No.	Reaction	A (m^3s^{-1})	b	E_a (eV)	α	Ref
^a X ₁ ^f	O ₂ + M → O + O + M	3.32×10^{-9}	-1.5	5.11	1	[36, 42, 44]
X ₂ ^f	O ₂ + N → NO + O	-	-	-		[38, 39]
^b X ₃ ^f	NO + O ₂ → NO ₂ + O	1.80×10^{-20}	0.58	1.96	1	[45]
^c X ₄ ^f	N ₂ + M → N + N + M	1.16×10^{-8}	-1.6	9.75	1	[35, 44]
X ₅ ^f	N ₂ + O → NO + N	-	-	-		[39, 40]
X ₆ ^f	NO ₂ + NO ₂ → NO + NO + O ₂	6.56×10^{-18}	0	1.20		[46]
^d X ₇ ^f	NO + M → N + O + M	3.32×10^{-15}	0	6.50		[44]
X ₈ ^f	NO + O + M → NO ₂ + M	^e 2.92×10^{-40}	-1.41	0		[47]

^a A is multiplied by 5.0 for M = N atom. The thermal rate coefficients for M = O₂ and O are derived from QCT data.

^b The rate coefficients for the reaction NO+O₂ are calculated using detailed balance, based on the rate coefficients of the reaction NO₂+O. The parameters A , b , and E_a are then fitted using the Arrhenius equation.

^c A is multiplied by 4.3 for M = O atom. The thermal rate coefficients for M = N₂ and N are derived from QCT data.

^d A is multiplied by 22 for atoms and NO, by 1.0 for other molecules, respectively.

^e The unit for three-body reactions is m^6s^{-1} .

where A is the pre-factor of the Arrhenius rate equation in Table 1, E_v [eV] is the vibrational energy at v^{th} vibrational level, α is the so-called ‘coefficient of vibrational energy utilisation’, taking a value between 0 and 1 [10], E_v^* is the effective vibrational energy of molecules, defined as the minimum value between E_v and $E_a\alpha^{-1}$, and Z is the vibrational partition function. More details on the procedure for calculating the non-thermal rate coefficients are reported by Shen *et al.* [41]. In this model, the rate coefficients of the forward reactions X₁^f–X₅^f can be enhanced by vibrational excitation.

A comparison of the state-specific reaction rate coefficients using the present method (Eq.6), the theoretical-informational (TI) method [10, 50], the Forced Harmonic Oscillator (FHO) method [51, 52], the Treanor-Marrone (TM) method ($U = 3T$) [53] and the QCT method [35, 36, 42] is shown in Figure 2. It is clear that the present method agrees best with the QCT calculation, which provides the most accurate data within this temperature range. However, the present method requires far less computational cost than the QCT method. A more detailed discussion of the various rate coefficients and how they compare was reported by Esposito [54].

The cumulative reaction product over time is calculated by:

$$M(t) = S \int R_i u dt \quad (7)$$

where the integration is performed along the PFR by summarizing the contributions of individual CSTRs. S [m^2] is cross-section area, R_i [$\text{m}^{-3}\text{s}^{-1}$] is the rate of reaction i , u

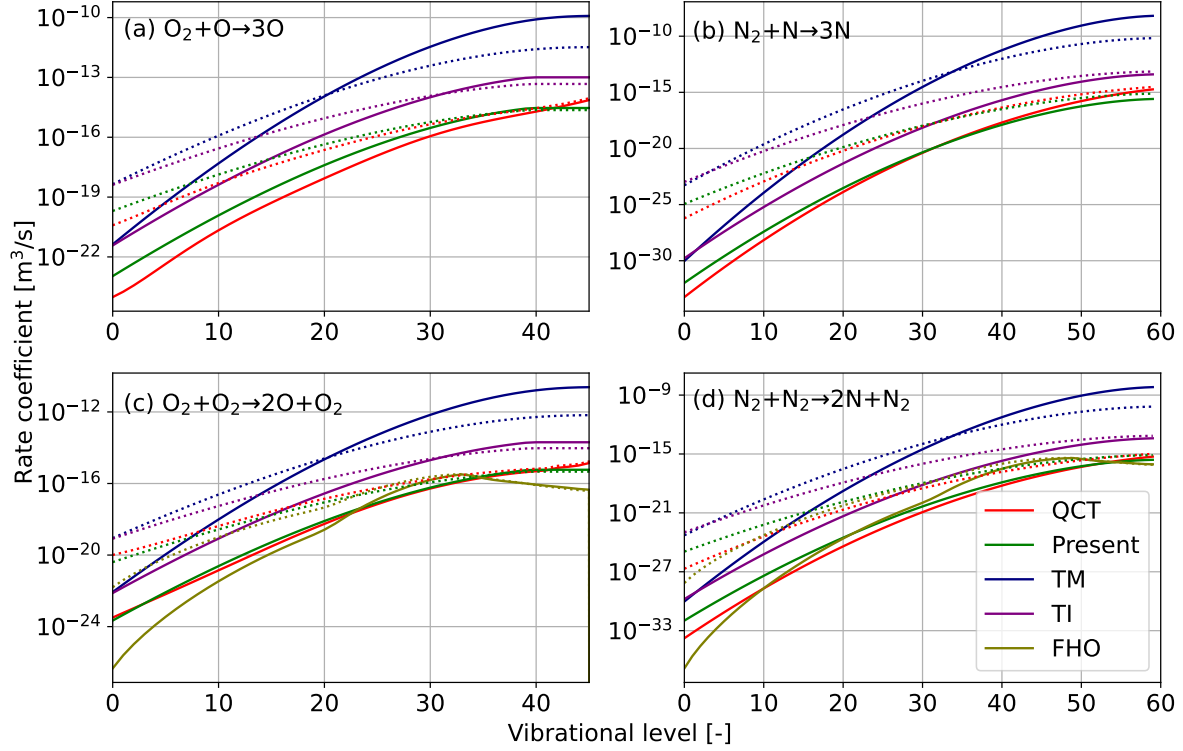


Figure 2: Comparison of V-D rate coefficients as a function of the vibrational level at different gas temperatures. Solid line: $T = 3000$ K; dotted line: $T = 5000$ K.

$[\text{m}\cdot\text{s}^{-1}]$ is the gas velocity, determined by local density and gas temperature:

$$u(t) = \frac{\dot{m}}{S\rho(t)} = \frac{N(t)RT(t)}{PA} \quad (8)$$

where ρ $[\text{kg}\cdot\text{m}^{-3}]$ is mass density, P [Pa] is pressure, N $[\text{mol}\cdot\text{m}^{-3}]$ is molar density, \dot{m} is mass flow rate, fixed at $0.00021 \text{ kg s}^{-1}$.

The continuity equation for the different species is [55]:

$$m \frac{dY_j}{dt} = \dot{m}(Y_{j,in} - Y_j) + V\dot{\omega}_j W_j \quad (9)$$

where $Y_{j,in}$ and Y_j are the mass fraction of species j in the inflow and outflow, respectively. $\dot{\omega}_j$ $[\text{mol}\cdot\text{m}^{-3}\text{s}^{-1}]$ and W_j $[\text{kg}\cdot\text{mol}^{-1}]$ are the molar production rate and molar mass of species j , respectively. m [kg] represents mass.

2.2. Vibrational kinetics

The vibrational excitation of N_2 and O_2 is recognized for its potential to lower the reaction barriers of the Zeldovich mechanism (reactions X_2^f and X_5^f in Table 1) [2, 6]. In this work, 60 vibrational levels of N_2 and 47 vibrational levels of O_2 are included, reported by Esposito *et al.* [36, 40] (Tables S1 and S2 in Supplementary material). The processes leading to vibrational excitation and de-excitation of molecular particles

by heavy particle impact, encompassing Vibration-Vibration (V-V) and Vibration-Translation (V-T) energy relaxation, are presented in Table 2. Many different methods have been developed to calculate the rate coefficients for V-V and V-T processes. The Schwartz–Slawsky–Herzfeld (SSH) method provided a theoretical framework for computing relaxation times in gases [56]. However, its accuracy is limited to single-quantum transitions and is insufficient for accurately calculating V-V and V-T rates at high vibrational levels and gas temperatures [57, 58]. To address these shortcomings, the FHO method, which was initially proposed by Kerner [59] and subsequently refined by Adamovich *et al.* [51] and Lino da Silva *et al.* [52], incorporates the coupling of many vibrational states during a collision, addressing the limitations of the SSH method [51, 60]. Unlike the SSH and FHO methods, which rely on the oscillator model, the QCT method offers a more comprehensive approach by considering realistic potential energy surfaces [39, 61]. It is important to note that while the QCT method provides superior accuracy, its prohibitive computational demands restrict its applicability [62]. To date, only a few databases for V-T relaxation have been calculated (*i.e.*, O₂-O and N₂-N), and comprehensive databases for other vibrational exchange rates using the QCT method are yet to be developed.

Table 2: List of vibrational kinetics processes. v_i and v_n are less than 60. v_j and v_m are less than 46. Backward rate coefficients are calculated using the principle of detailed balance.

Type	Process	Ref
V-T	$N_2(v_i) + N_2 \rightarrow N_2(v_i - \Delta v) + N_2, 1 \leq \Delta v \leq v_i$	[51]
V-T	$N_2(v_i) + O_2 \rightarrow N_2(v_i - \Delta v) + O_2, 1 \leq \Delta v \leq v_i$	[51]
V-T	$N_2(v_i) + N \rightarrow N_2(v_i - \Delta v) + N, 1 \leq \Delta v \leq \min(v_i, 50)$	[35]
V-T	$N_2(v_i) + O \rightarrow N_2(v_i - 1) + O$	[63]
V-T	$O_2(v_j) + O \rightarrow O_2(v_j - \Delta v) + O, 1 \leq \Delta v \leq \min(v_j, 30)$	[36]
V-T	$O_2(v_j) + O_2 \rightarrow O_2(v_j - \Delta v) + O_2, 1 \leq \Delta v \leq v_j$	[51]
V-T	$O_2(v_j) + N_2 \rightarrow O_2(v_j - \Delta v) + N_2, 1 \leq \Delta v \leq v_j$	[51]
V-V	$O_2(v_j) + N_2(v_i - 1) \rightarrow O_2(v_j - 1) + N_2(v_i)$	[51]
V-V	$O_2(v_j) + O_2(v_m - 1) \rightarrow O_2(v_j - 1) + O_2(v_m)$	[51]
V-V	$N_2(v_i) + N_2(v_n - 1) \rightarrow N_2(v_i - 1) + N_2(v_n)$	[51]

A comparison of single-quantum deactivation V-T rate coefficients using different methods is shown in Figure 3. The SSH calculations of V-T O₂-O₂ and N₂-N₂ processes [30, 57] exhibit better agreement with the quantum-classical (QC) calculations at low temperatures (below 1000 K). However, the SSH method fails to offer accurate results for the condition of interest in this work, since the gas temperature in the MW plasma typically exceeds several thousand Kelvin [23, 28]. Therefore, the FHO method is applied to compute the majority of V-T processes (involving O₂-O₂, O₂(v)-N₂, N₂-N₂, and N₂(v)-O₂), as well as all V-V processes considered in this study. All data

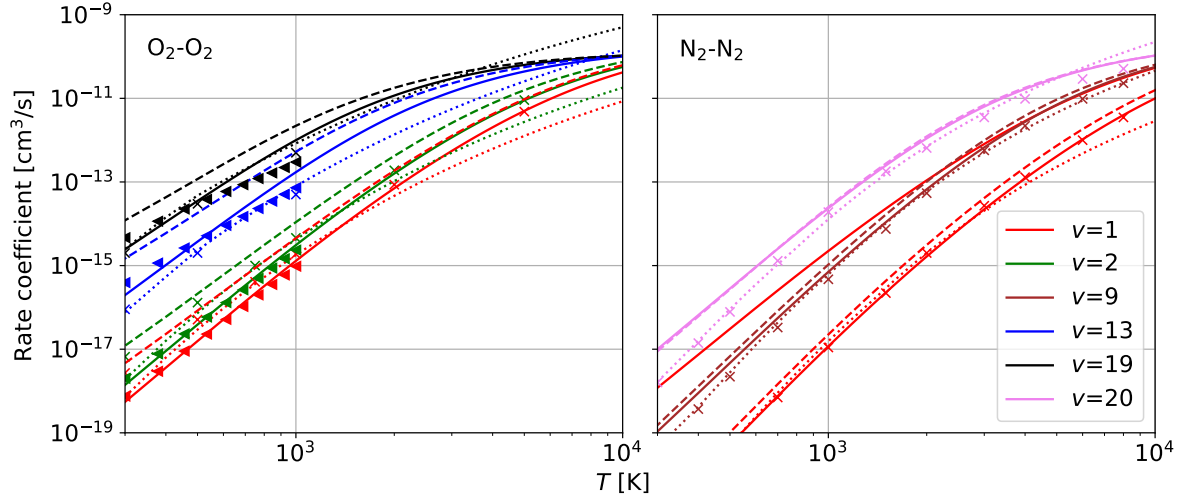


Figure 3: Comparison of available single-quantum V-T rate coefficients calculated by different methods as a function of the gas temperature. Solid line: FHO calculations by the present work; dotted line: SSH calculations by Guerra *et al.* and Kozak *et al.* [30, 57]; dashed line: FHO calculations by Lino da Silva *et al.* [64]; ×: The QC calculations by Billing *et al.* [65–67]; ▲: FHO calculations by Annušová *et al.* [58].

related to the FHO calculation, except for the vibrational energy of N_2 and O_2 at each vibrational level, can be found in the work of Adamovich *et al.* [51]. A striking difference is observed between the V-T deactivation rates of the first vibrational state for O_2 and N_2 , particularly at temperatures below 1000 K (as depicted by the red solid lines in Figure 3). O_2 exhibits notably faster vibrational deactivation than N_2 , primarily due to its smaller vibrational energy spacing in the molecular manifold. The discrepancy diminishes at higher temperatures.

The V-T $\text{N}_2\text{-O}$ process is considered to be one of the primary deactivation mechanisms, but the QCT results for the reaction rate are lower than the experimental results by orders of magnitude [22, 68]. Therefore, the V-T rate coefficients of the $\text{N}_2\text{-O}$ relaxation from the first vibrational state to the ground state is taken from Popov [63], which is fitted based on available experimental data [69–71]. Given the exceptionally high probabilities of the V-T $\text{N}_2\text{-O}$ process at elevated vibrational levels, the V-T rate coefficients at high levels are determined using the harmonic oscillator scaling law [72]. It means that only the single-quantum V-T $\text{N}_2\text{-O}$ relaxation processes are considered in the model. The gas-kinetic collision rates are introduced to assess the reasonableness of the V-T rate coefficients under varying conditions. All V-T rate coefficients remain lower than the gas-kinetic rate, even at very high temperatures (up to 10^4 K in this study) and elevated vibrational levels, as shown in Figure 4. Additionally, despite some deviations observed at lower temperatures and higher quantum numbers, in general the rate results align well with those obtained using the mixed quantum-classical (MQC) and Landau-Zener methods by Hong *et al.* [68]. To enhance accuracy, more rate coefficients for V-T $\text{N}_2\text{-O}$ processes are still needed, in particular to account for multi-quanta relaxation,

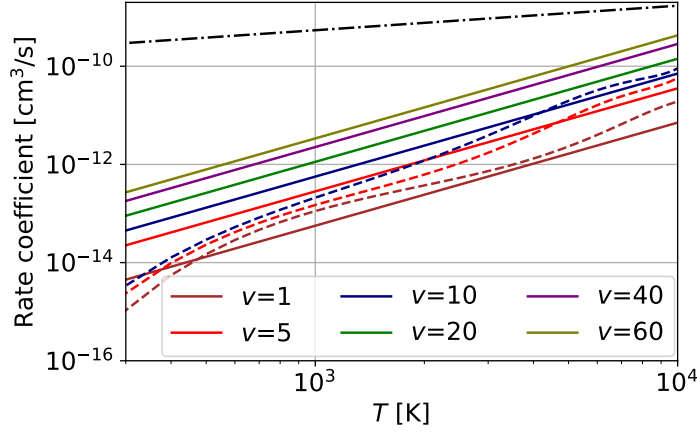


Figure 4: Evolution of single-quantum V-T N₂-O ($v \rightarrow v-1$) process as a function of gas temperature. Solid line: (scaled) fit of the experimental data [57, 63]; dashed line: results from Hong *et al.* [68]; dash-dotted line: the gas-kinetic collision rate [52].

using the MQC methods or other appropriate approaches.

For the V-T O₂-O and N₂-N processes, the interpolated data of the QCT method from Esposito *et al.* is used directly [35, 36]. Given the relatively weak non-equilibrium conditions studied in this work, the coexistence of N atoms with O₂ is rare under various conditions. Figures illustrating the time evolution of mole fractions in the quenching region at different initial temperatures and cooling rates can be found in Section 3.2 and Supplementary material. These figures also demonstrate the limited availability of N atoms coexisting with O₂ in the quenching region. Consequently, the V-T O₂-N process can be safely neglected in the simulation, thereby reducing computational costs.

In addition to single-quantum transitions, exploring the necessity of multi-quantum transitions in V-V and V-T processes is crucial for saving computational resources while maintaining accuracy (Figure 5). As the number of quanta increases, V-V rate coefficients exhibit a substantial decrease of nearly three orders of magnitude at different temperatures. Furthermore, it is worth noting that the computational cost required for the whole V-V process is significantly higher than that for the V-T process. For instance, with the inclusion of reverse relaxation reactions, the entire single-quantum V-V N₂-O₂ process encompasses 5104 reactions, whereas the entire single-quantum transition of the V-T N₂(v)-O₂ process covers only 116 reactions. Consequently, to address computational constraints, this study considers solely single-quantum V-V energy transition. For the V-T energy transition, while the rate coefficients of single-quantum transition consistently remain the highest, the differences in rate coefficients among various multi-quantum transitions are much smaller than those observed in the V-V processes, especially at high temperatures. Furthermore, it is important to note that, compared with the single-quantum V-T process, more vibrational energy can be dissipated in a multi-quantum V-T transition. Consequently, these processes can still play a significant role in vibrational energy relaxation. For instance, Figure S3 compares the energy

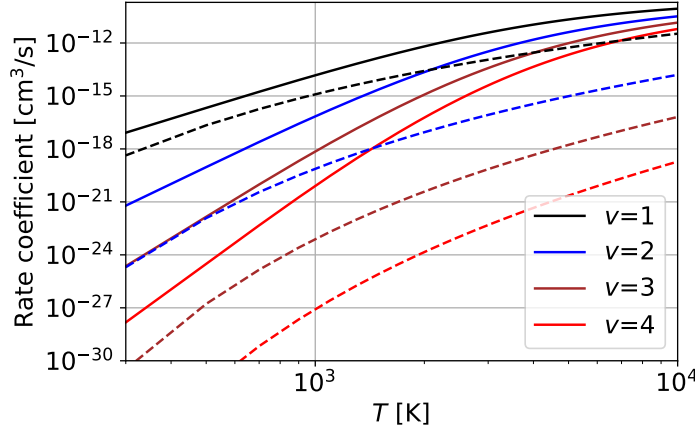


Figure 5: Vibrational relaxation N_2+O_2 collisions as a function of gas temperature. Solid line: V-T $\text{N}_2\text{-O}_2$ ($5 \rightarrow 5-v$) process; dashed line: V-V $\text{N}_2\text{-O}_2$ ($(5,0) \rightarrow (5-v,v)$) process.

transfer rates including V-T processes with different maximal numbers of quanta. The results emphasize the necessity of the multi-quantum V-T relaxation, especially at high temperatures. Therefore, nearly all the multi-quantum transitions in the V-T process are included in the model (Table 2).

2.3. Gas heating mechanisms

The heat exchange with the surroundings is the primary cooling mechanism in the model. The power density loss by external cooling is defined as [73, 74]:

$$Q_{wall} = c \frac{8\lambda}{r^2} (T - T_w) \quad (10)$$

where T_w is the wall temperature, fixed at 298.15 K, r is the reactor inner radius of the PFR (taken here as 13.5 mm), λ [$\text{W}(\text{m}\cdot\text{K})^{-1}$] represents the thermal conductivity. However, due to the influence of gas flow turbulence, the cooling rate in reality can be considerably higher [75]. Additionally, external factors such as using a nozzle [18, 20] or a water-cooled quenching rod [76] can further enhance the cooling in the afterglow. Therefore, a factor c ranging from 10 to 1000 is introduced to artificially raise the cooling rate in the model, making it more representative of experiments [73].

Based on the work of Kustova *et al.* [77], the vibrational thermal conductivity for species k is calculated by:

$$\lambda_k^{vib} = \frac{N_k C_{vib}^k}{\sum_j \frac{X_j}{D_{jk}}} \quad (11)$$

where N_k [$\text{mol}\cdot\text{m}^{-3}$] is the molar density of species k , X_k is the molar fraction of species k , D_{jk} [m^2s^{-1}] is the binary diffusion coefficient between species j and k , which depends on temperature and is calculated based on the Lennard-Jones binary interaction

potential [34, 78, 79]. C_{vib}^k [J(mol·K)⁻¹] is the vibrational molar heat capacity, which is equal to:

$$C_{vib}^k = N_A \frac{dE_{ave}^k}{dT_v^k} \quad (12)$$

where N_A is Avogadro's constant, and E_{ave}^k is the average vibrational energy [48], which is calculated by:

$$E_{ave}^k = \sum_v^{max} E_v^k f_v(T_v^k) \quad (13)$$

where E_v^k is the vibrational energy of N₂ or O₂ at the vibrational level v , and $f_v(T_v^k)$ is the Boltzmann factor based on the vibrational temperature.

A semi-empirical formula is used to calculate the thermal conductivity of the mixture λ_{mix} [31, 34, 80]:

$$\lambda_{mix} = \frac{1}{2} \left(\sum X_k \lambda_k + \frac{1}{\sum X_k / \lambda_k} \right) \quad (14)$$

where λ_k [W(m·K)⁻¹], is the pure species heat conductivity, and the coefficients of the polynomials are tabulated in the NASA library [81]. In order to exclude the contribution of the vibrational modes of N₂ and O₂, the pure-species thermal conductivity of N₂ and O₂ in Eq.14 should be replaced by λ_k^{tr-ro} , which is defined by Warnatz [79]:

$$\lambda_k^{tr-ro} = \lambda_k - N_k D_{kk} C_{vib}^k \quad (15)$$

where D_{kk} [in m²s⁻¹] is the self-diffusion coefficient, which is fitted by NASA [82]. All values in Eq.15 are relevant to T_g . Therefore, the power densities loss by external cooling relevant to vibrational and gas temperature are calculated by using different conductivities and temperatures based on Eq.11 and Eq.15, with sharing the same value of c in Eq.10.

Given that λ_{mix} depends on both the gas composition and gas temperature, the cooling rate is not constant within the quenching region. The cooling timescale is defined by the characteristic cooling time τ [s], over which the difference between the gas and wall temperatures becomes e times less than in the beginning. The average cooling rate \dot{T} [K/s] over this time is:

$$\dot{T} = \frac{T_g^0(1 - 1/e)}{\tau} \quad (16)$$

where T_g^0 [K] represents the initial gas temperature. Since the power density loss (Q_{wall}) due to external cooling depends on the temperature difference between the gas and wall temperatures, the relaxation time decreases with rising initial gas temperature. For different values of c (10, 100, and 1000), the average cooling rates are on the order of magnitude of 10⁶ K·s⁻¹, 10⁷ K·s⁻¹, and 10⁸ K·s⁻¹, respectively. For instance, as the initial gas temperature is 3000 K, the average cooling rates are 2.2×10⁶ K·s⁻¹, 2.1×10⁷ K·s⁻¹, and 1.8×10⁸ K·s⁻¹ under the conditions of $c=10$, 100, and 1000, respectively.

In the non-thermal quenching process, the difference between the gas temperature and vibrational temperatures necessitates consideration of both V-V and V-T processes. The processes involving electronically excited states are assumed to contribute negligibly to the vibrational power density in the quenching process. The vibrational temperature as a function of position is calculated by [32]:

$$NC_{vib}^{N_2(O_2)} \frac{dT_v^{N_2(O_2)}}{dt} = \frac{\dot{m}Y_{N_2(O_2),in}}{V} \left(h_{vib,in}^{N_2(O_2)} - h_{vib}^{N_2(O_2)} \right) + \sum Q_{chem-vib}^{N_2(O_2)} - \sum Q_{VV}^{N_2(O_2)+M} - \sum Q_{VT}^{N_2(O_2)+M} - Q_{wall}^{vib} \quad (17)$$

where $h_{vib,in}^{N_2(O_2)}$ [J·kg⁻¹] and $h_{vib}^{N_2(O_2)}$ [J·kg⁻¹] are the vibrational energy of inflow and outflow, respectively. $Q_{VT}^{N_2(O_2)+M}$ and $Q_{VV}^{N_2(O_2)+M}$ [W·m⁻³] are the vibrational power density exchange by related V-T and V-V processes of N₂ and O₂, separately (Table 2). Q_{wall}^{vib} represents the vibrational power density loss by conduction, based on Eq.10 and Eq.11. However, it should be stressed that this term could be overestimated at low temperatures due to slow surface vibrational relaxation [83, 84]. $\sum Q_{chem-vib}^{N_2(O_2)}$ [W·m⁻³] represents the total vibrational power density resulting from related chemical reactions for either O₂ or N₂, which contributes to raising or lowering the vibrational temperatures (Table 1). It is worth mentioning that vibrational energy can be both supplied by exothermic chemical reactions and consumed by endothermic chemical reactions. Therefore, it is essential to calculate how the released or consumed energy is distributed between vibrational and translational-rotational degrees of freedom. $\sum Q_{chem-vib}^{N_2}$ and $\sum Q_{chem-vib}^{O_2}$ can be expressed as:

$$\sum Q_{chem-vib}^{O_2} = E_b^{O_2} \sum_{m=1,2,3} (R_m^b \gamma_{rec}^m - R_m^f \gamma_{dis}^m) - E_{ave}^{O_2} \sum_{m=1,2,3} (R_m^b - R_m^f) \quad (18)$$

$$\sum Q_{chem-vib}^{N_2} = E_b^{N_2} \sum_{m=4,5} (R_m^b \gamma_{rec}^m - R_m^f \gamma_{dis}^m) - E_{ave}^{N_2} \sum_{m=4,5} (R_m^b - R_m^f) \quad (19)$$

where $E_b^{N_2}$ and $E_b^{O_2}$ are the bond energies (*i.e.*, potential energy of infinitely separated atoms relative to the ground vibrational state) of N₂ (9.75 eV) and O₂ (5.11 eV), m represent the number of reactions in Table 1.

The values of γ_{dis} (*i.e.*, the fraction of the bond energy provided by the vibrational energy in dissociation) can be determined based on the non-thermal rate coefficients:

$$\gamma_{dis} = \frac{\sum_i^{max} f_i(T_v^{N_2(O_2)}) k_i E_i^{N_2(O_2)}}{E_b^{O_2(N_2)} \sum_j^{max} f_j(T_v^{N_2(O_2)}) k_j} \quad (20)$$

where k_i [m³s⁻¹] is the state-specific rate coefficient at the i^{th} vibrational state. Due to the Boltzmann factor, γ_{dis} is affected not only by the gas temperature, but also by the vibrational temperature. Varied γ_{dis} values as functions of the gas temperature with different vibrational temperatures are shown in Figure 6. Due to the absence of complete QCT databases for the vibration-dissociation rate coefficients of N₂+O₂ and O₂+N₂ at different vibrational levels, the γ_{dis} of O₂+M and N₂+M are approximated

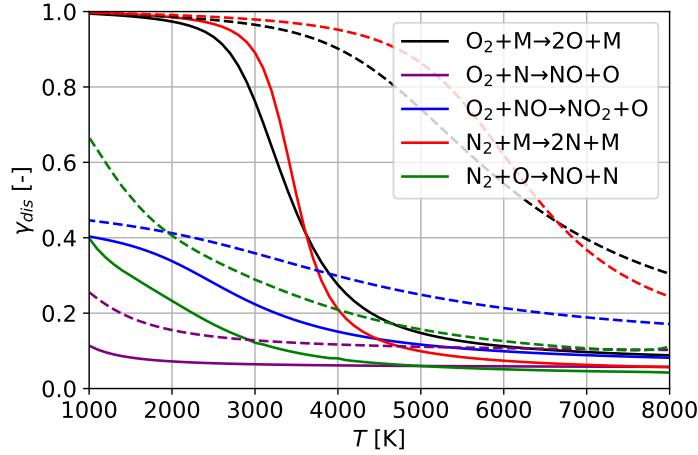


Figure 6: The fractions of the bond energy provided by vibrational energy in dissociation (γ_{dis}) for various reactions as a function of gas temperature at different vibrational temperatures. Solid line: $T_v = 3000$ K; dashed line: $T_v = 5000$ K. The γ_{dis} of O_2+M is determined as the average of the values for the reactions O_2+O and O_2+O_2 , derived from QCT data provided by Esposito *et al.* [36] and Andrienko *et al.* [42], respectively. The γ_{dis} of N_2+M is calculated as the average of the values for the reactions N_2+N and N_2+N_2 , based on QCT data from Esposito *et al.* [35]. The γ_{dis} of Zeldovich reactions N_2+O and O_2+N are derived using QCT data from Esposito *et al.* [40] and Armenise *et al.* [38, 39]. Additionally, the required non-thermal rate coefficients for the reaction $NO+O_2$ are calculated using the generalized Fridman-Macheret method [41].

using the average values of the reactions $O_2+O_2(O)$ and $N_2+N_2(N)$, separately. For the dissociation reactions O_2+M and N_2+M , nearly all the chemical energy is derived from vibrational energy when the vibrational temperature significantly exceeds the gas temperature. As the gas temperature rises above the vibrational temperature, both values of γ_{dis} decrease markedly. For the other three reactions (X_2^f , X_3^f , and X_5^f), the decrease in γ_{dis} with increasing gas temperature occurs when the gas temperature is considerably lower than the vibrational temperature. This difference in behaviour compared to the dissociation reactions can be explained by the activation barriers being lower than the bond energies.

The fraction of the bond energy converted to the vibrational energy in recombination (γ_{rec}) can be defined as:

$$\gamma_{rec} = \frac{\sum_i^{\max} \overleftarrow{k}_i E_i^{N_2(O_2)}}{E_b \sum_j^{\max} \overleftarrow{k}_j} \quad (21)$$

where \overleftarrow{k}_i [$m^3 s^{-1}$] is the backward state-specific rate coefficient at the i^{th} vibrational

state, calculated using the detailed balance principle:

$$\overleftarrow{k}_i = \frac{f_i(T_g) k_i}{K_{eq}} \quad (22)$$

Therefore, Eq.21 can be rewritten by:

$$\gamma_{rec} = \frac{\sum_i^{max} f_i(T_g) k_i E_i^{N_2(O_2)}}{E_b \sum_j^{max} f_j(T_g) k_j} \quad (23)$$

where γ_{rec} is influenced only by the gas temperature, and the value is equal to that of γ_{dis} under the thermal state (*i.e.*, $T_g = T_v^{N_2(O_2)}$). Consequently, γ_{rec} has the same value under both thermal and non-thermal conditions, provided the gas temperature is unchanged. As the gas temperature increases, reactions X_b^1 and X_b^4 show a slight decline in γ_{rec} , whereas the other reactions display an opposite trend, as illustrated in Figure 7.

Since the calculation of the V-T power density shares the same equation for different V-T processes, $Q_{VT}^{O_2-O_2}$ is considered as an example, which is equal to [74, 85]:

$$Q_{VT}^{O_2-O_2} = n_{O_2}^2 \left\{ \sum_r f_r(T_v^{O_2}) \left(\sum_w P_{r,w}^{O_2-O_2} \Delta E_{r,w}^{O_2} \right) \right\} \quad (24)$$

where $T_v^{O_2}$ [K] is the vibrational temperature of O_2 , $P_{r,w}^{O_2-O_2}$ [$m^3 s^{-1}$] and $\Delta E_{r,w}^{O_2}$ are the rate coefficients and the vibrational energy difference of the V-T O_2-O_2 process from r th vibrational level to w th level, respectively.

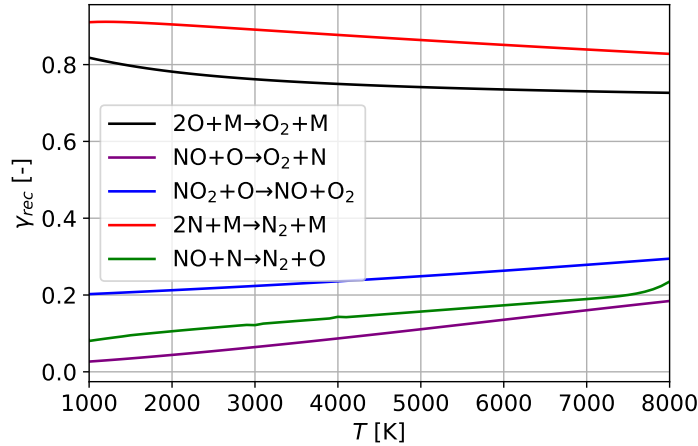


Figure 7: The fraction of the bond energy converted to the vibrational energy in recombination (γ_{rec}) for various reactions as a function of gas temperature.

Analogously, Q_{VV} [$W \cdot m^{-3}$] is the power density loss via the V-V process. Here, the vibrational power exchange of N_2 via the V-V N_2-O_2 process is considered as an example, defined by [74, 85]:

$$Q_{VV(N_2)}^{N_2-O_2} = n_{O_2} n_{N_2} \left\{ \sum_{i=0}^{\max-1} f_i(T_v^{O_2}) \left(\sum_{n=1}^{\max} P_{N_2(n,n-1)}^{O_2(i,i+1)} f_n(T_v^{N_2}) \Delta E_{n,n-1}^{N_2} \right) - \sum_{n=1}^{\max} f_n(T_v^{N_2}) \left(\sum_{i=0}^{\max-1} P_{N_2(n-1,n)}^{O_2(i+1,i)} f_i(T_v^{O_2}) \Delta E_{n+1,n}^{N_2} \right) \right\} \quad (25)$$

where $T_v^{N_2}$ [K] is the vibrational temperature of N_2 , $P_{N_2(n,n-1)}^{O_2(i,i+1)}$ and $P_{O_2(i+1,i)}^{N_2(n-1,n)}$ [m^3s^{-1}] are the corresponding forward and backward rate coefficients of the V-V N_2 - O_2 process, and both $\Delta E_{n,n-1}^{N_2}$ and $\Delta E_{n+1,n}^{N_2}$ are vibrational energy differences. It should be noted that due to the vibrational frequency difference between N_2 and O_2 , a part of the vibrational energy of N_2 is lost to gas heating via the V-V process. Additionally, due to unharmonicity, the varying energy gaps between adjacent vibrational levels also cause the corresponding V-V relaxation processes (*i.e.*, N_2 - N_2 and O_2 - O_2) to release part of the energy as direct gas heating.

The cumulative power loss of the V-V or V-T relaxation reaction i over time can be calculated by:

$$C_i(t) = A \int Q_{VT/VV}^i u dt \quad (26)$$

where the integration is performed along the PFR by summarizing the contribution of individual CSTRs.

Because the translational-rotational equilibrium occurs almost instantly, translational and rotational modes are grouped, governed by the gas temperature (*i.e.*, $T_g = T_{tr} = T_{rot}$) [10]. The calculation of the gas temperature is influenced by multiple factors, including chemical processes, conduction, V-T, and V-V relaxation processes. These factors collectively contribute to the dynamic evolution of the gas temperature during the quenching process [32]:

$$\begin{aligned} NC_P^{mix}(T_g) \frac{dT_g}{dt} = \frac{\dot{m}}{V} \left(h_{in} - \sum_j h_j Y_{j,in} \right) + \sum Q_{chem}^{heat} \\ - Q_{wall}^{mix} + \sum Q_{VV}^{heat} + \sum Q_{VT} \end{aligned} \quad (27)$$

where h_{in} [$J \cdot kg^{-1}$] and h_j [$J \cdot kg^{-1}$] represent the total species enthalpy of the inflow (excluding vibrational modes) and the species enthalpy of component j in the outflow (also excluding vibrational modes), respectively. $\sum Q_{VV}^{heat}$ and $\sum Q_{VT}$ are the sum of vibrational energy used for gas heating via all V-V and V-T relaxation processes, respectively. Q_{wall}^{mix} represents the power density loss of the gas mixture due to conduction, excluding contributions from the vibrational modes of N_2 and O_2 , C_P^{mix} [$J(mol \cdot K)^{-1}$] is the molar heat capacity of the gas mixture at constant pressure, excluding the vibrational modes of N_2 and O_2 , which is calculated by:

$$C_P^{mix}(T_g) = \sum_{i \neq N_2, O_2} X_i C_p^i(T_g) + X_{N_2} C_{p(ro-tr)}^{N_2}(T_g) + X_{O_2} C_{p(ro-tr)}^{O_2}(T_g) \quad (28)$$

where $C_p^i(T_g)$ [$J(mol \cdot K)^{-1}$] and X_i [-] are the molar heat capacity and molar fraction of all species except for N_2 and O_2 . For N_2 and O_2 , the molar heat capacity [$J(mol \cdot K)^{-1}$] of the rotational-translational mode is independent of temperature [82]. For the diatomic molecules N_2 and O_2 , the values of the molar heat capacity are both equal to $3.5R$ (where $1.5R$ comes from the translational component, $1R$ accounts for gas expansion, and $1R$ corresponds to the rotational component of diatomic species [82]). Finally,

Q_{chem}^{heat} [$\text{W}\cdot\text{m}^{-3}$] is the power density of the chemical energy converted for gas heating directly:

$$\sum Q_{chem}^{heat} = \sum Q_{chem} - \sum Q_{chem-vib}^{N_2} - \sum Q_{chem-vib}^{O_2} \quad (29)$$

where $\sum Q_{chem}$ represents the total power density released by all chemical reactions, calculated as follows:

$$\sum Q_{chem} = \sum_i R_i \Delta H_i \quad (30)$$

where ΔH_i [J] is enthalpy change between products and reactants, where the reaction enthalpies include the translational and rotational enthalpy of the species evaluated at the gas temperature, and the vibrational enthalpy of the species evaluated at the vibrational temperature (*i.e.* the average vibrational energy).

3. Results and discussion

3.1. Energy transfer and NO_x production in the plasma region

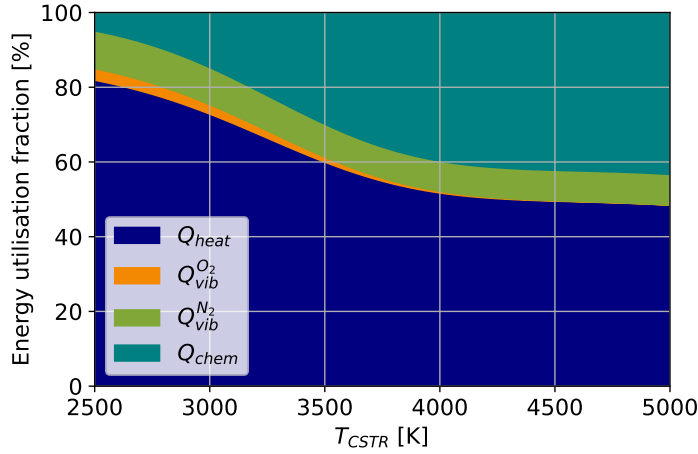


Figure 8: The energy utilisation fractions as a function of T_{CSTR} in the CSTR model at atmospheric pressure. Q_{heat} is the energy used for gas heating; Q_{chem} is the chemical energy; $Q_{vib}^{O_2}$ and $Q_{vib}^{N_2}$ are the vibrational energy of O_2 and N_2 , respectively.

As the initial air goes through the CSTR, which is considered to be in thermal equilibrium, a part of the heating power (in reality, provided by the MW radiation) is converted to chemical energy via chemical reactions, and heating is distributed uniformly over all degrees of freedom (Figure 8). As T_{CSTR} increases, an increasing fraction of O_2 dissociates into O atoms, resulting in a reduction of the vibrational energy of O_2 . With the assistance of active O atoms, the N_2 triple bond (9.75 eV) can be efficiently broken with an activation energy of 3.28 eV (reaction X_5^f). N atoms, produced in the above reaction, can subsequently react with O_2 to form NO (reaction X_2^f). Additionally, this reaction generates atomic oxygen, thus closing the chain of the Zeldovich mechanism [10].

Figure 9 illustrates the mole fractions of species and energy cost in the CSTR as a function of T_{CSTR} . The energy cost of the CSTR is calculated under the absolute quenching condition, *i.e.*, all the NO_x production in the CSTR can be retained during the quenching. Under this quenching condition, the optimal energy cost in the CSTR model is $2.6 \text{ MJ/mol N}^{-1}$ at 3110 K (Figure 9). The molar fraction results show excellent agreement with the thermodynamic equilibrium compositions calculated by D'Angola *et al.* [37]. One of the major challenges in the plasma nitrogen fixation process is its high energy cost [11]: even under optimal conditions, only 18% of the total energy is utilized for dissociation reactions (including those that are ineffective for synthesis), and the remainder is wasted on gas heating (Figure 8). Therefore, leveraging preheating by heat recovery and minimizing energy waste on gas heating are crucial steps to improve future performance [73, 86, 87].

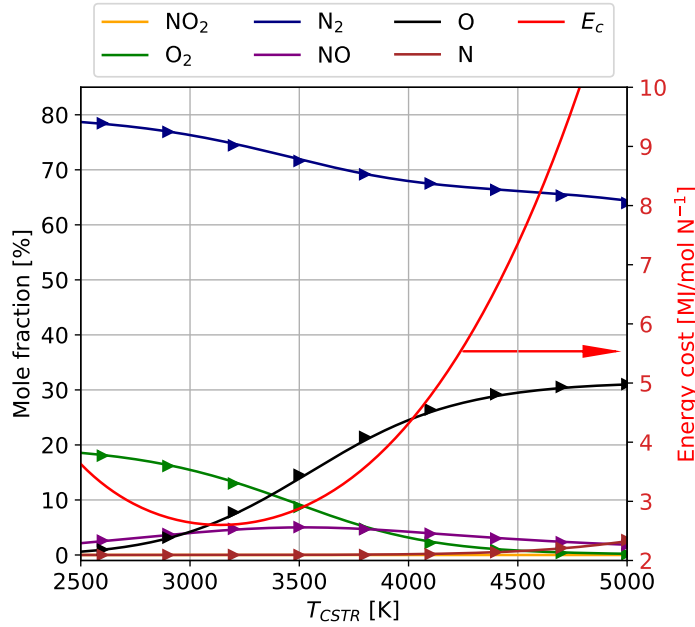


Figure 9: The mole fractions and energy cost as a function of the temperature in the CSTR under atmospheric pressure. Triangle symbols represent thermodynamic equilibrium compositions calculated by D'Angola *et al.* [37].

Once NO is formed, it can be further oxidized to NO_2 . However, nearly all the NO_2 produced by reaction X_3^{net} is consumed by reaction X_8^{net} . Therefore, the selectivity of NO is much higher than that of NO_2 in the plasma region. With temperature increasing, although high temperatures can break more N-N chemical bonds, NO is already destructed, which limits the energy efficiency for NO production at high temperatures in the CSTR. Additionally, limited O_2 availability at high temperatures, due to reaction X_1^f , constrains NO production by reaction X_2^f . As a result, the reaction X_5^f plays a dominant role in NO production at high temperatures. Above 4500 K , due to the depletion of O_2 , the vibrational energy of O_2 decreases to zero (Figure 8). Although

the amount of N_2 also decreases with higher temperature (Figure 9), a higher $T_v^{N_2}$ leads to the fraction of the vibrational energy of N_2 remaining stable.

3.2. Energy redistribution and chemical processes in the quenching process

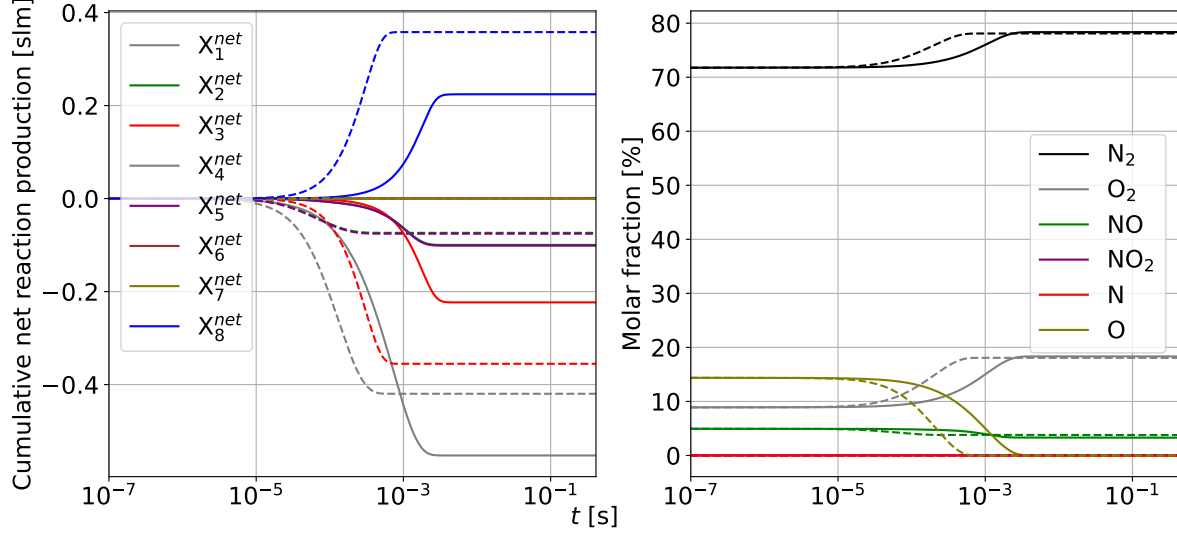


Figure 10: The cumulative net reaction product over different time intervals (based on Eq.7) and mole fractions as a function of the time in the quenching region with $T_{CSTR} = 3500$ K at different cooling rates. Solid: $c = 10$; dash: $c = 100$. X^{net} represents that both forward and backward reactions are taken into account.

With conduction to the wall, the gas temperature changes over time, triggering various reaction processes. To illustrate, the temporal evolution of the net production of various reactions and mole fractions of different species in the quenching process with $T_{CSTR} = 3500$ K and at different cooling rates is shown in Figure 10. With the low cooling rate ($c = 10$), 66.9% of O recombines to form O_2 , and 13.6% reacts with NO to form NO_2 . However, given that the reaction rate of X_3^b is faster than that of reaction X_8^f , nearly all of the NO_2 reacts with another 13.6% of O atoms to form NO and O_2 , leading to negligible net NO_2 formation until 0.1 s. A more detailed analysis of NO_2 formation is provided in the last section. The remaining (5.9%) O atoms trigger the reverse Zeldovich mechanism (reactions X_2^b and X_5^b), both of which reduce NO production. At a higher cooling rate ($c = 100$), over 95.5% of O atoms either recombine to form O_2 or react with NO and its subsequent products (*i.e.*, NO_2) to generate O_2 , effectively reducing NO loss via the reverse Zeldovich mechanism. Likewise, the results for higher T_{CSTR} (4500 K) can be found in Supplementary material.

Figure 11 depicts the temporal evolution of the energy utilisation fractions in the quenching process with $T_{CSTR} = 3500$ K at different cooling rates. At the start of the quenching process, which corresponds to the end of the CSTR, nearly 59% of the total energy is used for gas heating. Furthermore, a small amount of O_2 and most

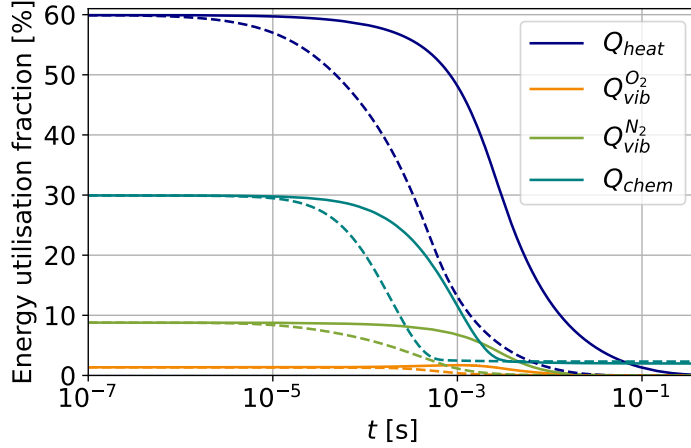


Figure 11: The energy utilisation as a function of time with $T_{CSTR} = 3500$ K at different cooling rates. Solid line: $c = 10$; dashed line: $c = 100$;

of the N_2 are still undissociated at the beginning of the quenching process (Figure 9), leading to 1% and 8% of the total energy still stored as vibrational energy in O_2 and N_2 , respectively. Due to the shorter characteristic cooling time (Figure 14) compared to vibrational-translational relaxation (τ_{vib}) and the characteristic time of chemical reactions (τ_{chem}), especially at high cooling rates, the translational-rotational energy relaxes faster than other forms of energy [88, 89]. Subsequently, more and more O atoms recombine (Figure 10), resulting in a portion of the recombination energy being converted to vibrational energy or heating the gas directly (Figure 11). Despite τ_{vib} being similar to τ_{chem} , this portion of chemical energy can keep the vibrational energy of O_2 unchanged or even slightly increase it before 0.1 ms. Because less chemical energy can convert to vibrational energy stored in N_2 than in O_2 , the vibrational energy of N_2 decreases faster during the quenching process. Eventually, only 1.9% and 2.2% of the total energy remains stored in the form of NO under the conditions of $c = 10$ and 100, respectively, which represents the energy efficiency for NO_x formation, while the rest of the energy is lost by heat transfer to the wall.

3.3. Analysis of the loss processes for vibrational energy

The time-dependent evolution of vibrational energy losses through different channels with $T_{CSTR} = 3500$ K at various cooling rates is illustrated in Figure 12. Under the condition of a low cooling rate ($c = 10$), most of the vibrational energy of N_2 is lost through conduction, accounting for 44.8%. Since V-V relaxation is less sensitive to gas temperature compared to V-T relaxation, it remains efficient for a longer duration. As a result, the V-V N_2 - O_2 process contributes nearly 28% to the vibrational energy loss of N_2 . Furthermore, 8.8% of the vibrational energy is converted into chemical energy, which is slightly lower than the energy lost via the V-T N_2 - O_2 process. Despite the similar relaxation rate coefficients between the V-T $N_2(v)$ - O_2 and N_2 - N_2 processes (Figure 5),

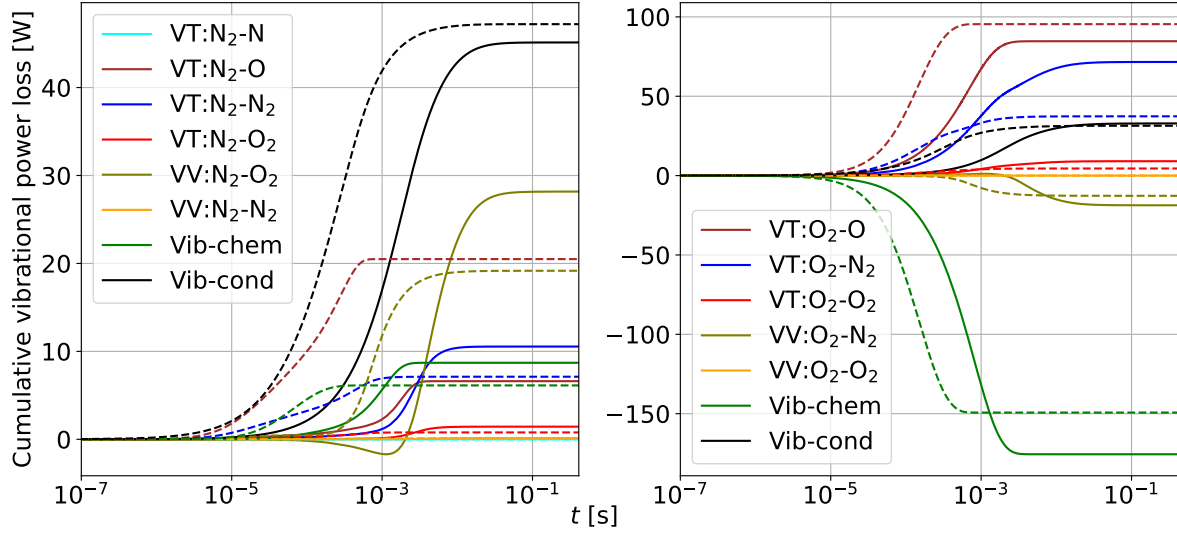


Figure 12: The cumulative vibrational energy loss of N_2 (left) and O_2 (right) by different channels over different time intervals in the quenching region with $T_{CSTR} = 3500$ K for different cooling rates, based on Eq.26. Solid: $c = 10$; dash: $c = 100$. The vib-chem term represents the total vibrational power loss contributed to all relevant chemical reactions. The vib-cond term denotes the vibrational power loss due to conduction.

the limited amount of O_2 restricts its contribution. Likewise, although the V-T N_2 -N process exhibits the highest relaxation rate coefficient at the same temperature, its contribution is similarly restricted due to the limited availability of N atoms. At a higher cooling rate ($c = 100$), a larger fraction of the vibrational energy of N_2 is dissipated through heat conduction. The onset of deactivation processes occurs approximately ten times faster, leading to the V-T N_2 -O process playing a more significant role, accounting for nearly 20% of vibrational energy loss. Consequently, the contributions of the V-V N_2 - N_2 process and the V-T N_2 - N_2 process to vibrational energy loss decrease.

Chemical energy released by relevant chemical reactions plays a vital role in enhancing the vibrational energy of O_2 in the quenching region. The V-T O_2 -O process consistently dominates the vibrational deactivation of O_2 across different cooling rates, especially at higher cooling rates, whereas the V-T $O_2(v)$ - N_2 and O_2 - O_2 processes exhibit the opposite trend (Figure 12). Notably, a portion of the vibrational energy of N_2 can be converted into that of O_2 through the V-V process, and the converted power decreases with higher cooling rate. Because of anharmonicity, V-V interactions of N_2 - N_2 and O_2 - O_2 result in some vibrational energy being lost, but the effects are limited (Figure 12).

In addition to the cooling rate, T_{CSTR} also influences the contributions of different relaxation processes (Figure 13). With an increase in T_{CSTR} in the plasma region, more recombination processes can occur in the afterglow, leading to more chemical energy being converted to vibrational energy. The increased number of O atoms in the plasma region at higher T_{CSTR} also promotes the V-T N_2 -O and O_2 -O processes

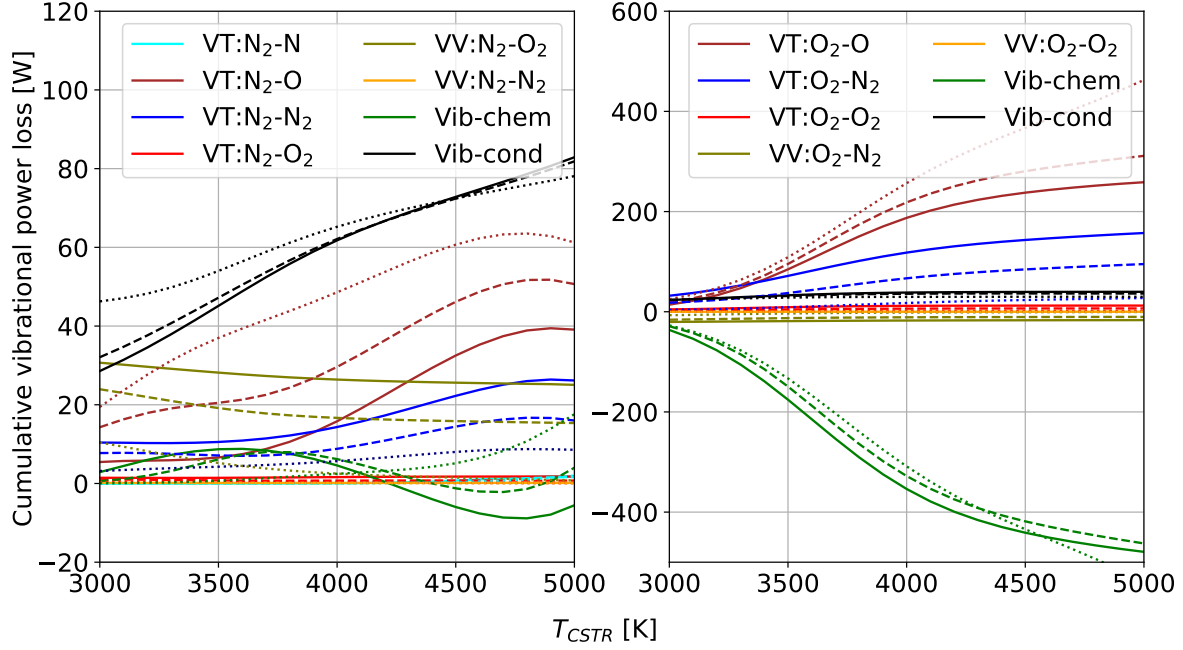


Figure 13: The cumulative vibrational energy loss of N_2 (left) and O_2 (right) by different channels in the whole quenching process as a function of T_{CSTR} at different cooling rates, based on Eq.26. Solid line: $c = 10$; dash line: $c = 100$; dot line: $c = 1000$. The vib-chem term represents the total vibrational power loss contributed to all relevant chemical reactions. The vib-cond term denotes the vibrational power loss due to conduction.

to become one of the dominant channels for the vibrational energy loss of N_2 and O_2 , respectively. Thermal conduction accounts for most of the vibrational energy loss of N_2 under most conditions but plays a limited role in the vibrational energy loss of O_2 . Although the V-T rate coefficients for $N_2(v)-O_2$ and O_2-O_2 increase significantly with rising gas temperature, the limited availability of reactants constrains their contributions to vibrational energy relaxation, particularly at high temperatures. Since the V-V N_2-O_2 process primarily affects the vibrational energy exchange between N_2 and O_2 at low gas temperatures (Figure 12), their contribution is not sensitive to T_{CSTR} and even slightly decreases with increasing T_{CSTR} . For the remaining deactivation processes, T_{CSTR} has a limited impact on their contribution to vibrational energy loss. As the cooling rate increases, more vibrational energy of N_2 and O_2 is consumed by the O atoms (*i.e.*, by V-T N_2-O and O_2-O processes). However, the cooling rate plays the opposite role in the contributions of $Q_{VT}^{N_2-N_2}$, $Q_{VT}^{O_2-N_2}$, and $Q_{VV}^{N_2-O_2}$.

3.4. Temporal variation of temperatures at different cooling rates

Since temperature affects both the chemical and the vibrational relaxation processes, modelling the gas temperature is of major importance [85]. Figure 14 reveals the temporal evolution of gas and vibrational temperatures. At a low cooling rate ($c =$

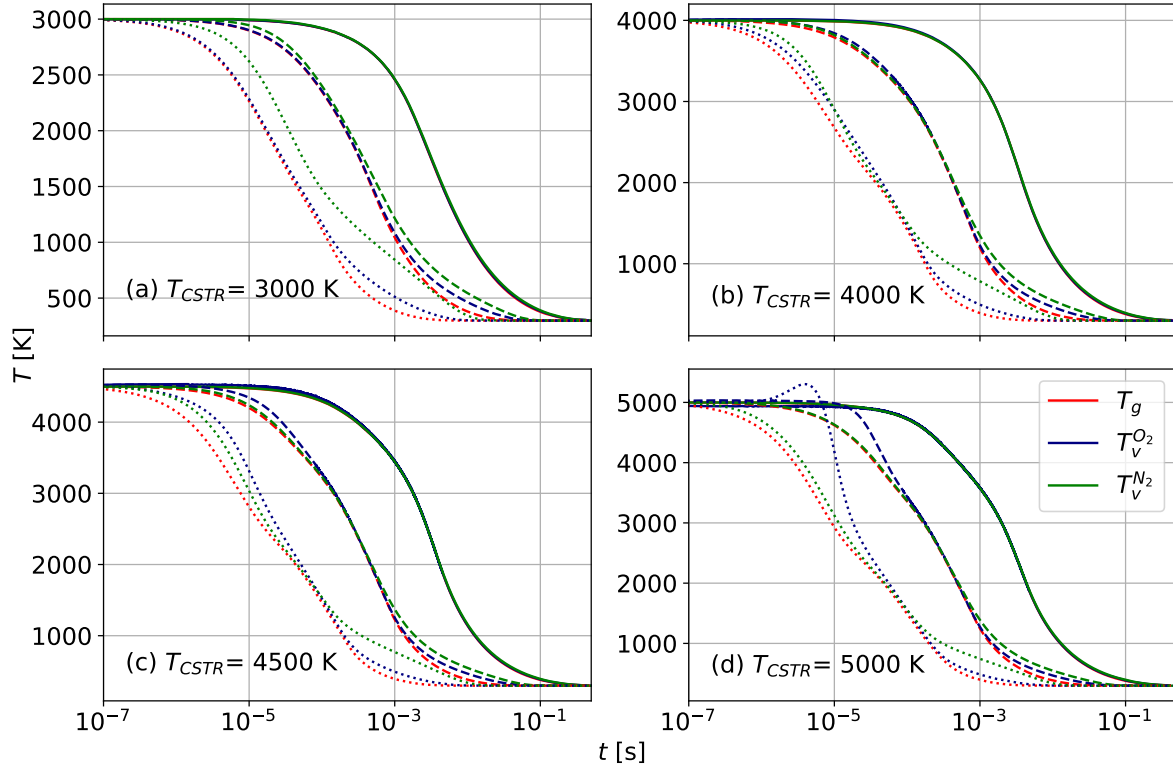


Figure 14: Temporal variation of the temperatures in the quenching process at different cooling rates and T_{CSTR} . Solid line: $c = 10$; dash line: $c = 100$; dot line: $c = 1000$.

10), all temperatures remain nearly in equilibrium throughout the entire quenching region. It is because V-T relaxation is sufficiently efficient to match the wall heat losses in the gas heat balance, leading to vibrational temperatures close to the gas temperature. Hence, it can be effectively replaced by a thermal quenching model, with much lower computational cost. As the cooling rate increases to $c = 100$ or even 1000, intensified cooling leads to a more rapid decline in gas temperature than in vibrational temperatures.

At the beginning of the quenching process with $T_{CSTR} = 3000$ K, the difference between $T_v^{O_2}$ and T_g is limited, but it increases as T_{CSTR} rises. The reason is that less O_2 is dissociated in the plasma region at low T_{CSTR} , which confines the supply of the vibrational energy of O_2 through the recombination reactions. Under the condition of $T_{CSTR} = 5000$ K, nearly all O_2 dissociates into O atoms in the plasma region (Figure 9), resulting in a high abundance of O atoms at the onset of the afterglow. Due to the high cooling rate, the rapid temperature drop triggers the recombination of O atoms, which releases a significant amount of chemical energy that is subsequently converted into the vibrational energy of O_2 . Due to the limited availability of O_2 at elevated temperatures, even a minor portion of the recombination energy can significantly enhance the vibrational temperature of O_2 during the initial quenching phase, when the vibrational energy generated from chemical energy exceeds that consumed by the

V-T relaxation processes. This leads to an increase in the vibrational temperature of O_2 at the beginning of the afterglow under the conditions of high cooling rate and T_{CSTR} .

In contrast to O_2 , the non-thermal behaviour of N_2 is more likely to occur under conditions of low T_{CSTR} and high cooling rates. The vibrational temperature of N_2 drops rapidly at high T_{CSTR} due to the deactivation effect by O atoms [90] through the V-T N_2 -O process. As O atoms disappear, the decrease in the vibrational temperature of N_2 slows during the latter half of the quenching process. It is noteworthy that, although a portion of the vibrational energy of N_2 is transferred to O_2 via the V-V O_2 - N_2 process in the later stages of quenching (Figure 12), conduction still limits the persistence of non-thermal behaviour in O_2 . As a result, the vibrational temperature of O_2 is closer to the gas temperature compared to that of N_2 .

3.5. Energy cost in the quenching process

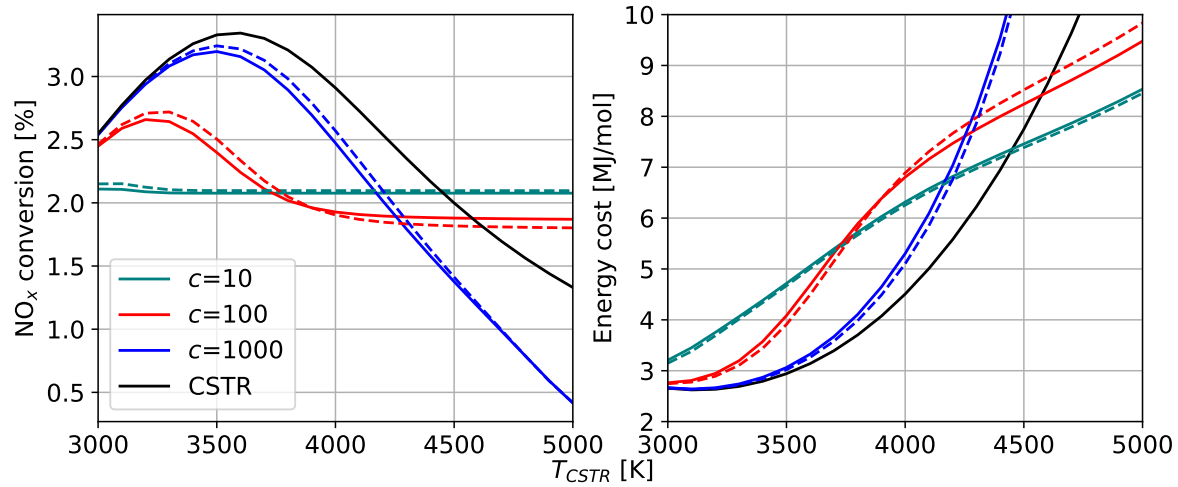


Figure 15: NO_x conversion and energy cost as a function of T_{CSTR} at different cooling rates. Solid line: non-thermal model; dash line: thermal model (*i.e.*, with $T_g = T_v^{N_2} = T_v^{O_2}$ and the heat balance equation with full thermodynamic properties).

In order to gain insight into the performance of the quenching process, the NO_x conversion and the energy cost as a function of T_{CSTR} at different cooling rates are investigated (Figure 15). Unlike plasma-activated CO_2 conversion, which requires a higher cooling rate in the quenching process [76], NO_x formation exhibits a more intricate relationship with the cooling rate. If T_{CSTR} ranges between 3000 K and 4200 K, a fast quenching process ($c = 1000$) can increase NO_x conversion and thereby decrease the energy cost. This improvement occurs because a high cooling rate can effectively reduce the detrimental effects of the reverse Zeldovich mechanism on NO production in the quenching region [7] (Figure 16). As a result, the highest conversion in the quenching region is 3.2% at 3500 K, while the lowest energy cost is 2.6 MJ/mol N^{-1} at 3110 K. Furthermore, the non-thermal effect emerges during quenching at higher cooling rates

Plasma type	Pressure	NO _x [%]	Energy cost [MJ/mol N ⁻¹]	Ref.
MW	1 atm	3.0	2.6	[2]
MW	≈1 atm	0.45	3.76	[91]
GA plasmatron	1 atm	1.4	3.8	[16]
Rotating GA	1 atm	2.5	3.0	[9]
Rotating GA	1 atm	0.8	2.7	[19]
Rotating GA	1 atm	3.9	3.5	[17]
Magnetic field glow discharge	1 atm	1.8	2.65	[92]
Magnetic field rotating GA	1 atm	1.3	4.2	[93]

Table 3: Experimental results of the nitrogen fixation yield and energy cost for different warm air (or N₂:O₂ = 4:1) plasma under (near) atmospheric pressure. The values quoted are obtained under various conditions.

(Figure 15), amplifying with increasing T_{CSTR} due to higher vibrational energy transfer by recombination heating (Figure 8). A relatively strong vibrational enhancement of NO_x production is observed at intermediate cooling rates, compared to low and high cooling rates. This is because a low cooling rate allows thermal equilibrium to be reached during quenching (Figure 14), while a high cooling rate causes vibrational temperatures to drop too quickly due to conduction, limiting vibrational energy for NO production within the timescale of chemical reactions. Despite this enhancement, the energy cost under the non-thermal state still fails to break the thermal limit of the CSTR under absolute quenching conditions across different cooling rates. With the optimal T_{CSTR} (*i.e.*, 3110 K), fast quenching ($c = 1000$) can preserve nearly all the NO_x produced in the plasma region. However, due to the constrained recombination energy (Figure 8), NO_x production enhanced by the non-thermal effect is very limited at the same T_{CSTR} . Table 3 reports the experimental energy cost of nitrogen fixation in (near) atmospheric warm air plasma under various conditions and plasma sources. The lowest energy cost found in all these experiments (~ 2.6 MJ/mol N⁻¹) is very similar to that predicted by the model presented under optimal conditions in this paper (Figure 15).

As the T_{CSTR} exceeds 3600 K, the NO loss through reverse Zeldovich reactions decreases with the low cooling rate ($c = 10$), while it continues to increase with higher cooling rates. Since the reaction rate coefficients of X₂^f are similar to that of X₅^b at high temperatures but much lower than that of X₅^b at low temperatures, a low cooling rate can extend the high-temperature region and thus enhance the reaction time of N atoms with O₂. Thus, with a low cooling rate, N atoms produced in the plasma region are able to combine with more O₂, which minimizes the destruction of NO within the quenching region. Consequently, the energy cost with the low cooling rate ($c = 10$) becomes lower than that with $c = 100$ (at 3770 K) and $c = 1000$ (at 4200 K), respectively. When T_{CSTR} exceeds 4450 K, the higher NO production by the reactions X₂^{net} and X₇^{net}, in comparison to the NO loss via the reaction X₅^{net}, boosts NO production at $c = 10$ in the quenching process, thereby reducing the energy cost after quenching. However, the higher cooling rate results in lower net NO production via the reactions X₂^{net}, coupled

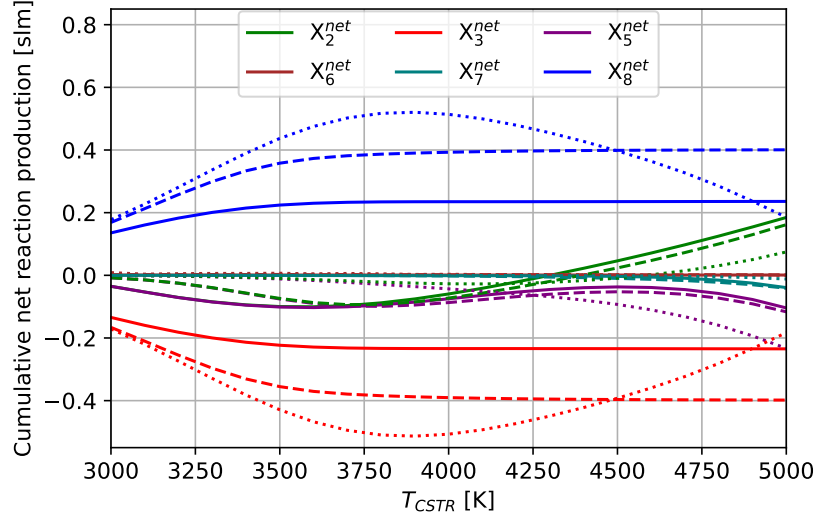


Figure 16: The cumulative net reaction production related to NO and NO₂ formation in the whole quenching process as a function of T_{CSTR} at different cooling rates, based on Eq.7. Solid line: $c = 10$; dash line: $c = 100$; dot line: $c = 1000$. X^{net} represents that both forward and backward reactions are taken into account.

with higher NO loss through the reactions X_5^{net} and X_7^{net} . In summary, the optimal cooling rate for NO_x formation depends strongly on T_{CSTR} . While fast quenching can enhance NO_x production for moderate temperatures (3000–4200 K), it becomes less beneficial for higher temperatures due to the reversed Zeldovich reactions. Consequently, careful optimisation of both T_{CSTR} and cooling rate is essential to achieve efficient NO_x production and thus reduce energy cost.

The model indicates that non-thermal effects have a limited influence on the afterglow of air plasma at atmospheric pressure. However, it is expected to be more applicable at lower pressures. In MW plasma, where the reduced electric field typically ranges from 10 to 100 Td [94], most electron energy is transferred to the vibrational excitation of N₂ [95]. As pressure decreases, the impact of V-T relaxation processes weakens, leading to more pronounced non-thermal effects. Considering that strong non-thermal effects have been observed in the experiment at low pressures [96], the non-thermal effects may also persist in the quenching region, potentially enhancing NO production. Furthermore, diffusion effects become more significant at lower pressures, resulting in less steep temperature gradients [97], making the 1D axial model a more suitable approximation for such conditions.

Besides NO, NO₂ is another product of interest, primarily affected by reactions X_3^{net} , X_6^{net} , and X_8^{net} in this study. As previously discussed, the high temperature within the CSTR significantly limits NO₂ production (Figure 9). At the beginning of the quenching process, where most recombination processes take place, nearly all the NO₂ generated by reaction X_8^f is consumed by reaction X_3^b (Figure 16), providing an effective pathway for oxygen recombination. Nearly all NO₂ forms in the later part of

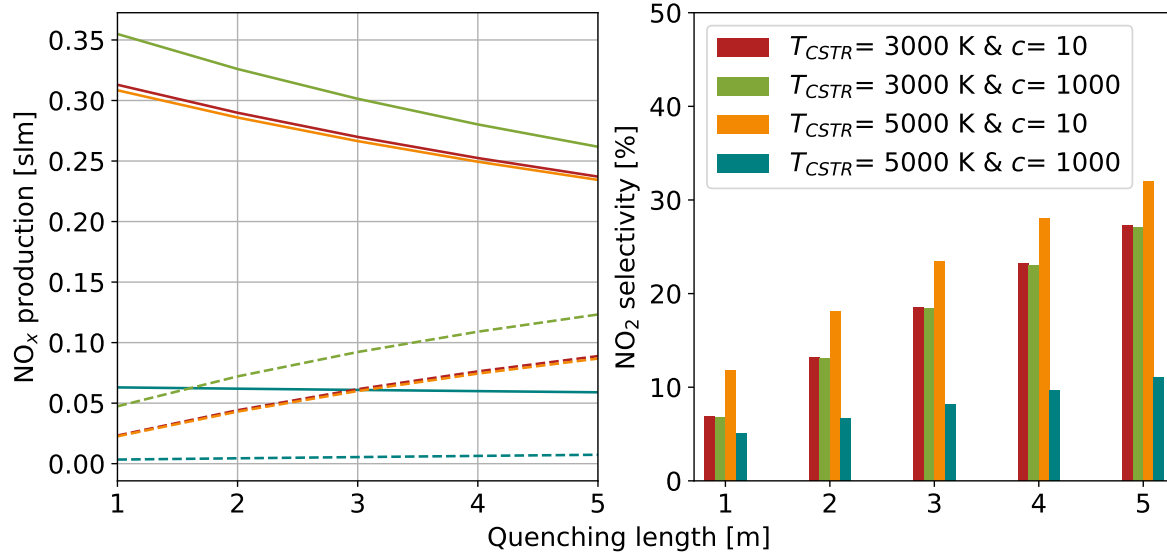


Figure 17: NO₂ selectivity and NO_x production as a function of quenching length under different conditions. Solid line: NO production; dash line: NO₂ production; column data: NO₂ selectivity.

the quenching process, primarily facilitated by reaction X_6^b , which is relatively slow and operates optimally at lower gas temperatures. The production and selectivity of NO₂ as a function of quenching length under various conditions are illustrated in Figure 17. Notably, NO₂ selectivity exhibits a positive correlation with residence time. The influence of the cooling rate and T_{CSTR} on NO₂ production is less pronounced compared to that of residence time. Furthermore, under conditions of high T_{CSTR} and high cooling rate ($T_{CSTR} = 5000$ K and $c = 1000$), the limited NO production constrains reaction X_6^b , leading to a lower NO₂ selectivity. Given that reaction X_6^b is exothermic, its progression does not require additional thermal excitation. Therefore, with an infinitely long residence time, all NO will eventually convert to NO₂ if sufficient O₂ is available, reaching chemical equilibrium. This suggests that the key to maximizing NO₂ production lies in extending the residence time to ensure sufficient reaction time for NO₂ formation processes, particularly at lower temperatures in the quenching region where reaction X_6^b is most effective.

4. Conclusions

The primary aim of this study is to investigate the energy transfer mechanisms and NO_x formation that occur during the quenching process of dry air MW plasma at atmospheric pressure. A 1D multitemperature chemical kinetics model that incorporates a common translational-rotational temperature and separate vibrational temperatures for N₂ and O₂, connected through various vibrational excitation and relaxation reactions, is introduced. Given the inherent limitations of the 1D model, it is incapable of

simulating temperature gradients in the radial direction. Consequently, the primary objective of this study is not to replicate exact experimental data but to serve as a crucial first step toward optimizing plasma reactors for efficient NO_x production.

Firstly, the properties of the thermal plasma region is analysed using the CSTR model, demonstrating that chemical equilibrium is reached at typical plasma lengths. It is observed that the lowest energy cost in the plasma region is $2.6 \text{ MJ/mol N}^{-1}$ at a gas temperature in the plasma region of $T_{CSTR} = 3110 \text{ K}$. However, more than 81% of the total energy is dissipated for gas heating at the same time.

The downstream model shows that the optimal cooling rate in the quenching region depends on T_{CSTR} . At relatively low T_{CSTR} values (3000–4200 K), a higher cooling rate enhances O_2 recombination, which reduces NO loss through the reverse Zeldovich mechanism. Consequently, the optimal conditions for NO formation are found at the optimal T_{CSTR} (3110 K) and with rapid quenching (characterized by $c = 1000$). However, due to the limited recombination energy at the optimal T_{CSTR} , the non-thermal effects during quenching cannot further facilitate NO formation or overcome the thermal limit. At higher T_{CSTR} values (above 4200 K), a lower cooling rate allows the mixture to remain longer in the optimal temperature range for NO formation, which can potentially reduce the energy cost. Therefore, at a low cooling rate, more N atoms can combine with O_2 rather than reacting with NO, which occurs at a higher cooling rate. Compared to low and high cooling rates, a greater vibrational enhancement of NO_x production occurs under intermediate cooling rate conditions. Although non-thermal effects have a limited influence on the afterglow of air plasma at atmospheric pressure, we believe the application of this model to lower-pressure conditions can bring invaluable insight, where non-thermal effects are more pronounced.

Thirdly, the impact of various vibrational energy loss processes of N_2 and O_2 in the quenching region is analyzed. The predominant factors limiting vibrational non-equilibrium for N_2 and O_2 are vibrational heat conduction and the V-T O_2 -O process, respectively. As T_{CSTR} increases, aided by higher V-T relaxation rates and more dissociated oxygen in the plasma region, V-T O_2 -O and N_2 -O processes consume more vibrational energy of O_2 and N_2 . The V-V N_2 - O_2 process undertakes a more significant role in the vibrational energy exchange of N_2 with low T_{CSTR} . The model also predicts how different temperatures evolve over time under varying cooling rates during the quenching process.

Finally, the NO_2 formation in the plasma and quenching regions is discussed, separately. Due to the higher rate coefficients of the reaction $\text{NO}_2 + \text{O}$, all the NO_2 formed by the reaction of $\text{NO} + \text{O} + \text{M}$ is consumed by O atoms in the plasma region and the early part of the quenching region, where T_g remains high. The model results highlight the reaction of $2\text{NO} + \text{O}_2$ as the primary driver of NO_2 formation. This reaction requires sufficient residence time and low gas temperature to proceed effectively.

5. Acknowledgement

This work was financially supported by the China Scholarship Council (Grant No. CSC202106240037). VG was partially supported by FCT – Fundação para a Ciência e Tecnologia under the projects UIDB/50010/2020 (<https://doi.org/10.54499/UIDB/50010/2020>), UIDP/50010/2020 (<https://doi.org/10.54499/UIDP/50010/2020>), LA/P/0061/2020 (<https://doi.org/10.54499/LA/P/0061/2020>), and PTDC/FIS-PLA/1616/2021 (<https://doi.org/10.54499/PTDC/FIS-PLA/1616/2021>). The author sincerely thanks Lex Kuijpers for their valuable assistance in polishing the English language of this article.

6. Supplementary material

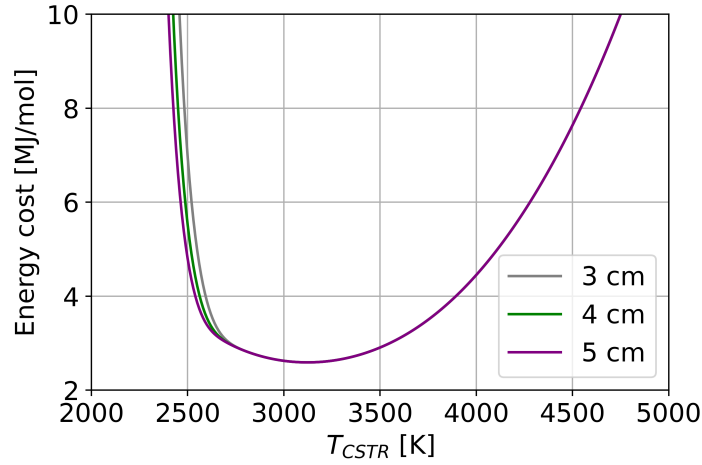


Figure S1: Energy cost in the plasma length as a function of T_{CSTR} at different plasma lengths under atmospheric pressure.

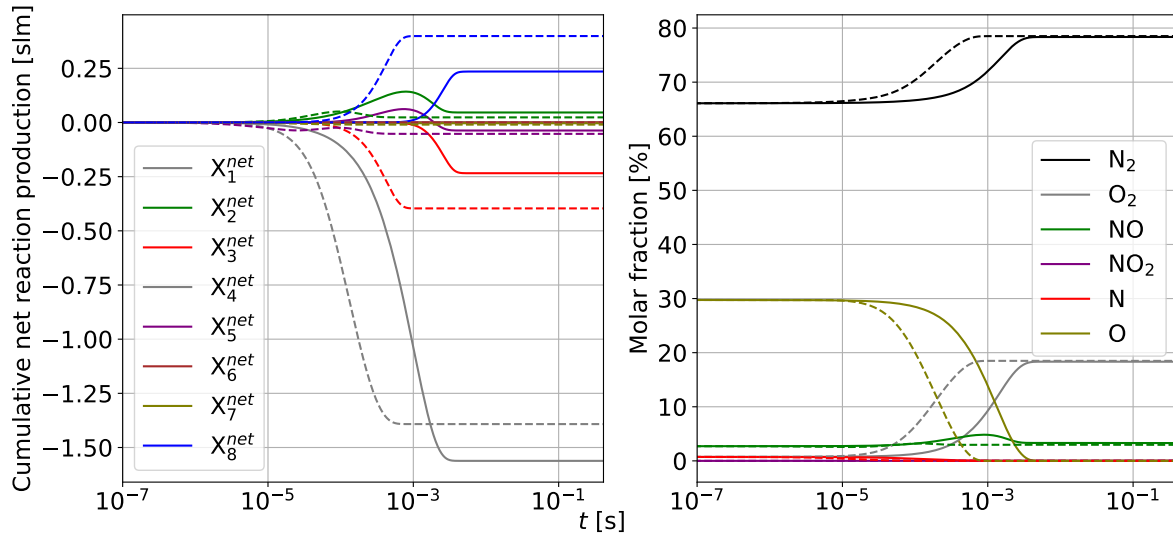


Figure S2: The net reaction production and mole fractions as a function of the time in the quenching region with $T_{CSTR} = 4500$ K at different cooling rates. Solid: $c = 10$; dash: $c = 100$. X^{net} means considering both forward and backward reaction effects.

Table S1: O₂ vibrational levels and the corresponding energies at the respective ground rotational levels [36].

v	E_v (eV)	v	E_v (eV)	v	E_v (eV)	v	E_v (eV)	v	E_v (eV)
0	0.09745	10	1.03779	20	2.99673	30	4.52001	40	5.09830
1	0.29065	11	1.21788	21	3.13813	31	4.60590	41	5.13293
2	0.48125	12	1.39517	22	3.27583	32	4.68674	42	5.16100
3	0.66941	13	1.56956	23	3.40973	33	4.76239	43	5.18243
4	0.85490	14	1.74104	24	3.53983	34	4.83271	44	5.19735
5	1.03779	15	1.90934	25	3.66583	35	4.89753	45	5.20638
6	1.21788	16	2.07464	26	3.78783	36	4.95668	46	5.21082
7	1.39517	17	2.23674	27	3.90563	37	5.00998		
8	1.56956	18	2.39554	28	4.01922	38	5.05725		
9	1.74104	19	2.55104	29	4.12852	39	5.09830		

Table S2: N₂ vibrational levels and the corresponding energies at the respective ground rotational levels [40].

v	E_v (eV)	v	E_v (eV)	v	E_v (eV)	v	E_v (eV)	v	E_v (eV)
0	0.151726	13	3.605168	26	6.367745	39	8.410388	52	9.646625
1	0.441947	14	3.842309	27	6.551098	40	8.535777	53	9.703346
2	0.728036	15	4.075379	28	6.730192	41	8.656395	54	9.753875
3	1.010007	16	4.304370	29	6.905002	42	8.772182	55	9.797986
4	1.287873	17	4.529277	30	7.075500	43	8.883070	56	9.835412
5	1.561646	18	4.750090	31	7.241657	44	8.988990	57	9.865829
6	1.831331	19	4.966799	32	7.403441	45	9.089864	58	9.888824
7	2.096939	20	5.179395	33	7.560820	46	9.185609	59	9.903833
8	2.358474	21	5.387863	34	7.713757	47	9.276135	60	9.913001
9	2.615942	22	5.592189	35	7.862214	48	9.361342		
10	2.869344	23	5.792359	36	8.006151	49	9.441121		
11	3.118683	24	5.988354	37	8.145524	50	9.515353		
12	3.363958	25	6.180156	38	8.280286	51	9.583904		

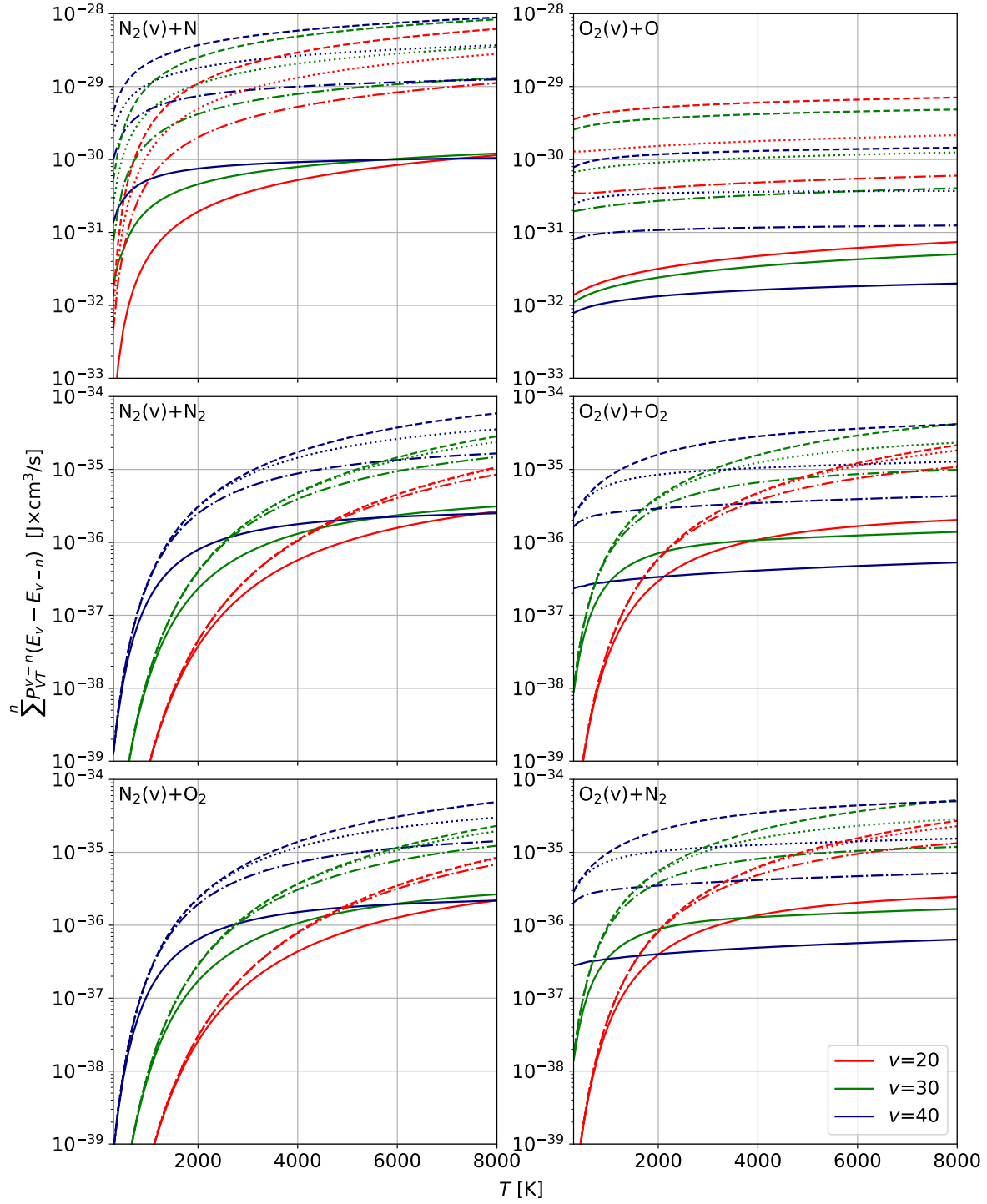


Figure S3: Comparison of the energy transfer rates including V-T processes with different maximal numbers of quanta. Solid line: $n = 1$ (*i.e.*, only single quantum V-T relaxation is considered); dash-dotted line: $n = 5$; dotted line: $n = 10$; dash line: $n = 20$.

References

- [1] Patil B, Wang Q, Hessel V and Lang J 2015 *Catalysis today* **256** 49–66
- [2] Kelly S and Bogaerts A 2021 *Joule* **5** 3006–3030
- [3] Smith C, Hill A K and Torrente-Murciano L 2020 *Energy & Environmental Science* **13** 331–344
- [4] Rouwenhorst K H, Jardali F, Bogaerts A and Lefferts L 2021 *Energy & environmental science* **14** 2520–2534
- [5] Wang W, Patil B, Heijkers S, Hessel V and Bogaerts A 2017 *ChemSusChem* **10** 2145–2157
- [6] Winter L R and Chen J G 2021 *Joule* **5** 300–315
- [7] Abdelaziz A A, Teramoto Y, Nozaki T and Kim H H 2023 *ACS Sustainable Chemistry & Engineering* **11** 4106–4118
- [8] Li D, Zan L, Chen S, Shi Z J, Chen P, Xi Z and Deng D 2022 *National Science Review* **9** nwac042
- [9] Jardali F, Van Alphen S, Creel J, Eshtehardi H A, Axelsson M, Ingels R, Snyders R and Bogaerts A 2021 *Green Chemistry* **23** 1748–1757
- [10] Fridman A 2008 *Plasma chemistry* (Cambridge university press)
- [11] Liu J, Nie L, Liu D and Lu X 2024 *Plasma Processes and Polymers* **21** 2300153
- [12] Asisov R, Givotov V, Rusanov V and Fridman A 1980 *Sov. Phys* **14** 366
- [13] Muzammil I, Lee D H, Dinh D K, Kang H, Roh S A, Kim Y N, Choi S, Jung C and Song Y H 2021 *RSC advances* **11** 12729–12738
- [14] Bogaerts A and Neyts E C 2018 *ACS Energy Letters* **3** 1013–1027
- [15] Snoeckx R and Bogaerts A 2017 *Chemical Society Reviews* **46** 5805–5863
- [16] Vervloessem E, Aghaei M, Jardali F, Hafezkhiaani N and Bogaerts A 2020 *ACS Sustainable Chemistry & Engineering* **8** 9711–9720
- [17] Tsonev I, O’Modhrain C, Bogaerts A and Gorbaney Y 2023 *ACS Sustainable Chemistry & Engineering* **11** 1888–1897
- [18] Van Alphen S, Eshtehardi H A, O’Modhrain C, Bogaerts J, Van Poyer H, Creel J, Delplancke M P, Snyders R and Bogaerts A 2022 *Chemical engineering journal* **443** 136529
- [19] Majeed M, Iqbal M, Altin M, Kim Y N, Dinh D K, Lee C, Ali Z and Lee D H 2024 *Chemical Engineering Journal* **485** 149727
- [20] van Deursen C, van Poyer H, Bongers W, Peeters F, Smits F and van de Sanden M 2024 *Journal of CO₂ Utilization* **88** 102952
- [21] Mercer E R, Van Alphen S, Van Deursen C, Righart T, Bongers W, Snyders R, Bogaerts A, Van De Sanden M and Peeters F 2023 *Fuel* **334** 126734
- [22] Esposito F 2022 *Plasma Sources Science and Technology* **31** 094010

- [23] Altin M, Viegas P, Vialetto L, van de Steeg A, Longo S, van Rooij G and Diomede P 2022 *Plasma Sources Science and Technology* **31** 104003
- [24] Altin M, Viegas P, Vialetto L, van Rooij G and Diomede P 2024 *Plasma Sources Science and Technology* **33** 045008
- [25] Kustova E, Nagnibeda E, Alexandrova T Y and Chikhaoui A 2002 *Chemical physics* **276** 139–154
- [26] Shizgal B D and Lordet F 1996 *The Journal of chemical physics* **104** 3579–3597
- [27] Cutler A, Magnotti G, Cantu L, Gallo E, Danehy P, Baurle R, Rockwell R, Goynes C and McDaniel J 2012 Measurement of vibrational nonequilibrium in a supersonic freestream using dual-pump cars *28th Aerodynamic Measurement Technology, Ground Testing, and Flight Testing Conference including the Aerospace T&E Days Forum* p 3199
- [28] Tatar M, Vashisth V, Iqbal M, Butterworth T, van Rooij G and Andersson R 2024 *Chemical Engineering Journal* **497** 154756
- [29] Bongers W, Bouwmeester H, Wolf B, Peeters F, Welzel S, van den Bekerom D, den Harder N, Goede A, Graswinckel M, Groen P W *et al.* 2017 *Plasma processes and polymers* **14** 1600126
- [30] Kozák T and Bogaerts A 2014 *Plasma Sources Science and Technology* **23** 045004
- [31] Kee R J, Coltrin M E and Glarborg P 2005 *Chemically reacting flow: theory and practice* (John Wiley & Sons)
- [32] Goodwin D G, Moffat H K, Schoegl I, Speth R L and Weber B W 2023 Cantera: An object-oriented software toolkit for chemical kinetics, thermodynamics, and transport processes <https://www.cantera.org> version 3.0.0
- [33] Kotov V and Koelman P M 2019 *Plasma sources science and technology* **28** 095002
- [34] Vialetto L, van de Steeg A, Viegas P, Longo S, van Rooij G J, van de Sanden M, van Dijk J and Diomede P 2022 *Plasma Sources Science and Technology* **31** 055005
- [35] Esposito F, Armenise I and Capitelli M 2006 *Chemical Physics* **331** 1–8
- [36] Esposito F, Armenise I, Capitta G and Capitelli M 2008 *Chemical Physics* **351** 91–98
- [37] D’angola A, Colonna G, Gorse C and Capitelli M 2008 *The European Physical Journal D* **46** 129–150
- [38] Armenise I and Esposito F 2021 *Chemical Physics* **551** 111325
- [39] Armenise I 2023 *Chemical Physics* **571** 111937
- [40] Esposito F and Armenise I 2017 *The Journal of Physical Chemistry A* **121** 6211–6219
- [41] Shen Q, Pikalev A, Peeters F J, Gans J and van de Sanden M C 2024 *Reaction Chemistry & Engineering*
- [42] Andrienko D A and Boyd I D 2017 *Chemical Physics* **491** 74–81

- [43] Kotov V, Kiefer C K and Hecimovic A 2023 *Plasma Sources Science and Technology*
- [44] Johnston C and Brandis A 2014 *Journal of Quantitative Spectroscopy and Radiative Transfer* **149** 303–317
- [45] Atkinson R, Baulch D, Cox R, Hampson Jr R F, Kerr J and Troe J 1989 *Journal of Physical and Chemical Reference Data* **18** 881–1097
- [46] Konnov A A 2009 *Combustion and Flame* **156** 2093–2105
- [47] Yarwood G, Sutherland J, Wickramaaratchi M and Klemm R 1991 *The Journal of Physical Chemistry* **95** 8771–8775
- [48] Andrienko D A and Boyd I D 2015 *Physics of Fluids* **27** 116101
- [49] Lino da Silva M, Guerra V and Loureiro J 2007 *Chemical Physics* **342** 275–287
- [50] Berthelot A and Bogaerts A 2018 *Journal of CO₂ Utilization* **24** 479–499
- [51] Adamovich I V, Macheret S O, Rich J W and Treanor C E 1998 *Journal of Thermophysics and Heat Transfer* **12** 57–65
- [52] Lino da Silva M 2007 *Journal of Thermophysics and Heat Transfer* **21** 40–49
- [53] Capitelli M, Esposito F, Kustova E and Nagnibeda E 2000 *Chemical Physics Letters* **330** 207–211
- [54] Esposito F and Armenise I 2021 *The Journal of Physical Chemistry A* **125** 3953–3964
- [55] See <https://cantera.org/stable/reference/reactors/ideal-gas-constant-pressure-reactor.html>
- [56] Schwartz R, Slawsky Z and Herzfeld K 1952 *The Journal of Chemical Physics* **20** 1591–1599
- [57] Guerra V, Tejero-Del-Caz A, Pintassilgo C D and Alves L L 2019 *Plasma Sources Science and Technology* **28** 073001
- [58] Annušová A, Marinov D, Booth J P, Sirse N, Lino da Silva M, Lopez B and Guerra V 2018 *Plasma Sources Science and Technology* **27** 045006
- [59] Kerner E H 1958 *Canadian Journal of Physics* **36** 371–377
- [60] Adamovich I V, Macheret S O, Rich J W and Treanor C E 1995 *AIAA journal* **33** 1064–1069
- [61] Andrienko D A and Boyd I D 2018 *Journal of Thermophysics and Heat Transfer* **32** 904–916
- [62] Lino da Silva M, Guerra V and Loureiro J 2009 *Plasma Sources Science and Technology* **18** 034023
- [63] Popov N 2011 *Journal of Physics D: Applied Physics* **44** 285201
- [64] See <http://esther.ist.utl.pt/pages/stellar.php> for STELLAR database
- [65] Billing G D and Kolesnick R 1992 *Chemical Physics Letters* **200** 382–386
- [66] Billing G D and Fisher E 1979 *Chemical Physics* **43** 395–401

- [67] Billing G D 1994 *Chemical physics* **179** 463–467
- [68] Hong Q, Bartolomei M, Pirani F, Esposito F, Sun Q and Coletti C 2022 *Plasma Sources Science and Technology* **31** 084008
- [69] Breshears W and Bird P 1968 *The journal of chemical physics* **48** 4768–4773
- [70] Eckstrom D 1973 *The Journal of Chemical Physics* **59** 2787–2795
- [71] McNeal R, Whitson Jr M and Cook G 1974 *Journal of Geophysical Research* **79** 1527–1531
- [72] Guerra V and Loureiro J 1995 *Journal of Physics D: Applied Physics* **28** 1903
- [73] Vermeiren V and Bogaerts A 2020 *The Journal of Physical Chemistry C* **124** 18401–18415
- [74] Pintassilgo C, Guerra V, Guaitella O and Rousseau A 2014 *Plasma Sources Science and Technology* **23** 025006
- [75] Belov I, Vermeiren V, Paulussen S and Bogaerts A 2018 *Journal of CO₂ Utilization* **24** 386–397
- [76] Kim H, Song S, Tom C P and Xie F 2020 *Journal of CO₂ Utilization* **37** 240–247
- [77] Kustova E and Nagnibeda E 2006 *Chemical physics* **321** 293–310
- [78] Synek P, Obrusník A, Hübner S, Nijdam S and Zajíčková L 2015 *Plasma Sources Science and Technology* **24** 025030
- [79] Kee R J, Dixon-Lewis G, Warnatz J, Coltrin M E and Miller J A 1986 *Sandia National Laboratories Report SAND86-8246* **13** 80401–1887
- [80] Mathur S, Tondon P and Saxena S 1967 *Molecular physics* **12** 569–579
- [81] McBride B J 1993 *Coefficients for calculating thermodynamic and transport properties of individual species* vol 4513 (NASA Langley Research Center)
- [82] Gupta R N, Yos J M, Thompson R A and Lee K P 1990
- [83] Black G, Wise H, Schechter S and Sharpless R L 1974 *The Journal of Chemical Physics* **60** 3526–3536
- [84] Marinov D, Lopatik D, Guaitella O, Hübner M, Ionikh Y, Röpcke J and Rousseau A 2012 *Journal of Physics D: Applied Physics* **45** 175201
- [85] Pintassilgo C D and Guerra V 2016 *The Journal of Physical Chemistry C* **120** 21184–21201
- [86] Sarafraz M, Christo F, Tran N, Fulcheri L and Hessel V 2023 *International Journal of Hydrogen Energy* **48** 6174–6191
- [87] Patil B S, Peeters F, van Rooij G J, Medrano J, Gallucci F, Lang J, Wang Q and Hessel V 2018 *AIChE Journal* **64** 526–537
- [88] Kosareva A, Kunova O, Kustova E and Nagnibeda E 2022 *Physics of Fluids* **34**
- [89] Kosareva A, Kunova O, Kustova E and Nagnibeda E 2021 *Physics of Fluids* **33**
- [90] Silva T, Bera S, Pintassilgo C D, Herrmann A, Welzel S, Tsampas M N, van de Sanden M C, Alves L L and Guerra V 2024 *The Journal of Physical Chemistry A* **128** 7235–7256

- [91] Kim T, Song S, Kim J and Iwasaki R 2010 *Japanese journal of applied physics* **49** 126201
- [92] Li Z, Nie L, Liu D and Lu X 2022 *Plasma Processes and Polymers* **19** 2200071
- [93] Chen H, Wu A, Mathieu S, Gao P, Li X, Xu B Z, Yan J and Tu X 2021 *Plasma Processes and Polymers* **18** 2000200
- [94] Viegas P, Vialetto L, Wolf A, Peeters F, Groen P, Righart T, Bongers W, Van de Sanden M and Diomede P 2020 *Plasma Sources Science and Technology* **29** 105014
- [95] Li Z, Wu E, Nie L, Liu D and Lu X 2023 *Physics of Plasmas* **30**
- [96] Samadi Bahnamiri O, Verheyen C, Snyders R, Bogaerts A and Britun N 2021 *Plasma Sources Science and Technology* **30** 065007
- [97] Wolf A, Righart T, Peeters F, Groen P, Van De Sanden M and Bongers W 2019 *Plasma Sources Science and Technology* **28** 115022